

Accepted Manuscript

Frictional melt homogenisation during fault slip: Geochemical, textural and rheological fingerprints

Paul A. Wallace, Sarah Henton De Angelis, Adrian J. Hornby, Jackie E. Kendrick, Stephen Clesham, Felix W. von Aulock, Amy Hughes, James E. P. Utley, Takehiro Hirose, Donald B. Dingwell, Yan Lavallée

PII: S0016-7037(19)30217-0
DOI: <https://doi.org/10.1016/j.gca.2019.04.010>
Reference: GCA 11205

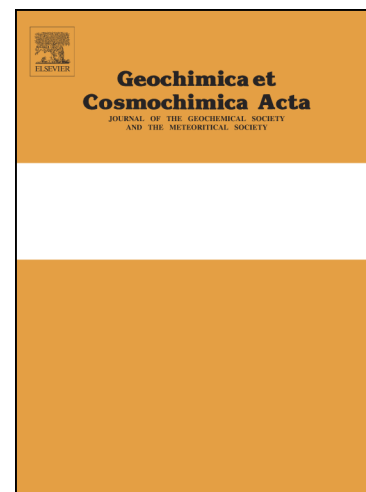
To appear in: *Geochimica et Cosmochimica Acta*

Received Date: 14 October 2018

Accepted Date: 6 April 2019

Please cite this article as: Wallace, P.A., Henton De Angelis, S., Hornby, A.J., Kendrick, J.E., Clesham, S., von Aulock, F.W., Hughes, A., E. P. Utley, J., Hirose, T., Dingwell, D.B., Lavallée, Y., Frictional melt homogenisation during fault slip: Geochemical, textural and rheological fingerprints, *Geochimica et Cosmochimica Acta* (2019), doi: <https://doi.org/10.1016/j.gca.2019.04.010>

This is a PDF file of an unedited manuscript that has been accepted for publication. As a service to our customers we are providing this early version of the manuscript. The manuscript will undergo copyediting, typesetting, and review of the resulting proof before it is published in its final form. Please note that during the production process errors may be discovered which could affect the content, and all legal disclaimers that apply to the journal pertain.



Frictional melt homogenisation during fault slip: Geochemical, textural and rheological fingerprints

Paul A. Wallace ^{a,*}, Sarah Henton De Angelis ^a, Adrian J. Hornby ^{a,c}, Jackie E. Kendrick ^a, Stephen Clesham ^a, Felix W. von Aulock ^a, Amy Hughes ^a, James E. P. Utley ^a, Takehiro Hirose ^b, Donald B. Dingwell ^c and Yan Lavallée ^a

^a *Department of Earth, Ocean and Ecological Sciences, University of Liverpool, Liverpool L69 3GP, United Kingdom.*

^b *Kochi Institute for Core Sample Research (KCC), Japan Agency for Marine-Earth Science and Technology (JAMSTEC), 200 Monobe-otsu, Kochi, Nankoku 783-8502, Japan*

^c *Earth and Environmental Sciences, Ludwig-Maximilians-Universität (LMU), Theresienstrasse 41/III, 80333 Munich, Germany*

*Corresponding author: *Paul.Wallace@liverpool.ac.uk*

Abstract

Volcanic environments often represent structurally active settings where strain localisation can promote faulting, frictional deformation, and subsequent melting along fault planes. Such frictional melting is thermodynamically a disequilibrium process initiated by selective melting of individual mineral phases and softening of volcanic glass at its glass transition as a response to rapid frictional heating. The formation of a thin melt layer on a fault plane surface can drastically accelerate or terminate slip during fault motion. A comprehensive understanding of the physical and chemical properties of the frictional melt is required for a full assessment of slip mechanism, as frictional rheology depends on the contributions from selectively melted mineral and glass phases as well as the physical effects of restite fragments suspended in the frictional melt. Here, we experimentally investigate the impact of host-rock mineralogy on the compositional and textural evolution of a frictional melt during slip. High-velocity rotary shear (HVR) experiments were performed under controlled, volcanically relevant, coseismic conditions (1 m s⁻¹ slip rate and 1 MPa normal stress) using three intermediate dome lavas with contrasting mineral assemblages, sampled from volcanic

systems where fault friction is evident: (1) an amphibole-bearing andesite (Soufrière Hills Volcano, Montserrat); (2) an amphibole-poor dacite (Santiaguito dome complex, Guatemala); and (3) an amphibole-free andesite (Volcán de Colima, Mexico). For each sample, five HVR experiments were terminated at different stages of frictional melt evolution, namely: (1) at the onset of melting and (2) formation of a steady-state melt layer; and (3) after 5 m, (4) 10 m, and (5) 15 m of slip at steady-state conditions. Progressive mixing and homogenisation of selective, single-phase melts within the frictional melt layer through double-diffusion convection demonstrates the dependence of melt composition on slip behaviour. Amphiboles melted preferentially, leading to lower shear stress (~ 1 MPa) and pronounced shear weakening during the frictional melting of amphibole-bearing lavas. The results highlight the implications of mineral assemblage on volcanic conduit flow processes, which may influence the explosivity of eruptions, and run-out distances of rapid granular flows.

Keywords: Amphibole; Chemical homogenisation; Faulting; Frictional melt; Viscosity; Volcano

1. Introduction

1.1. Frictional melting

Frictional melting is a highly dynamic and chemically chaotic phenomenon associated with coseismic faulting and slip as a manifestation of extreme strain localisation (e.g., Sibson, 1975; Allen, 1979; Magloughlin and Spray, 1992; O'Hara, 1992). The presence of a thin melt layer on a narrow slip plane—commonly inferred to be generated at strain-rates $> 10^{-2} \text{ s}^{-1}$ and slip velocities $> 0.1 \text{ m s}^{-1}$ —is an important control on slip properties (Spray, 1992). The generation of such melts is a thermomechanical response to energy dissipation associated with the conversion of friction-induced deformation to heat (i.e., frictional heating). This process often results in a quasi-linear melt layer that is preserved in the geologic record as a pseudotachylyte, providing kinematic evidence for coseismic faulting activity (e.g., Shand, 1916; Francis, 1972; Sibson, 1975; Di Toro et al., 2006).

Experimental work has demonstrated the mechanical influence of frictional melting on slip dynamics in geological materials (e.g., Lin and Shimamoto, 1998; Hirose and Shimamoto, 2005; Di Toro et al., 2006; Niemeijer et al., 2011; Kendrick et al., 2014b; Hornby et al., 2015). These studies have highlighted that the evolution of a frictional melt with slip displacement can dictate a material's

frictional behaviour. Frictional melts can act as either (1) a lubricant, drastically reducing the frictional resistance during slip (e.g., McKenzie and Brune, 1972; Tsutsumi and Shimamoto, 1997), or (2) a viscous brake, causing slip velocity to wane and seismic slip to terminate (e.g., Koizumi et al., 2004; Kendrick et al., 2014b).

The physical properties of the host material (e.g., surface interface roughness; Nielsen et al., 2010; Harbord et al., 2017) and its constituent minerals (e.g., melting point and shear strength; Spray, 1992) influence the progression of frictional melting. Owing to rapid heating during fault slip—several hundred degrees over a few seconds of slip (e.g., McKenzie and Brune, 1972; Lavallée et al., 2012; Kendrick et al., 2014b; Hornby et al., 2015)—frictional melting is considered a non-equilibrium adiabatic process involving the selective melting of individual mineral phases in the order of their solidus temperatures (e.g., Scott and Drever, 1953; Sibson, 1975; Spray, 1992; Lin and Shimamoto, 1998). In particular, the presence of hydrous phases (e.g., phyllosilicates, amphiboles) can significantly enhance melting probability owing to their lower melting points and the associated release of H₂O (Allen, 1979).

The geochemical signatures of natural pseudotachylytes and experimentally-derived frictional melts demonstrate their derivation from selective melting of the host material (Magloughlin, 1992; O'Hara, 1992; Spray, 1992; Hetzel et al., 1996; Lavallée et al., 2012; Jiang et al., 2015). Furthermore, it has been proposed that the compositional evolution of frictional melts may be used to constrain source properties and slip duration (Jiang et al., 2015), but a systematic experimental and geochemical approach has yet to be undertaken.

The shear resistance exerted by frictional melts during slip is strongly influenced by their rheological properties (i.e., viscosity and strain-rate; e.g., Hirose and Shimamoto, 2005; Lavallée et al., 2012; Hornby et al., 2015). Work on the viscosities of multicomponent silicate melts has resulted in a statistically robust dataset over a wide compositional range, all displaying strong non-Arrhenian temperature-dependence and highlighting chemical composition, temperature and strain-rate as key controls on rheology (Hess and Dingwell, 1996; Giordano et al., 2008). During frictional melting, only phases with melting temperatures higher than the formation temperature of the melt can survive, leaving a suspension of remnant crystals. Substantial work has demonstrated the influence of

suspended crystals on non-Newtonian viscosity and parameterisations have been generated (e.g., Caricchi et al., 2007; Costa et al., 2009; Cimarelli et al., 2011; Lavallée et al., 2012; Mader et al., 2013).

1.2. Fault friction in volcanic environments

Volcanic systems display abundant evidence for fault activity. For example, faulting can take place during the ascent of high-temperature, high-viscosity magma within the shallow volcanic conduit (e.g., Tuffen and Dingwell, 2005; Hale and Wadge, 2008; Kendrick et al., 2012; Lavallée et al., 2013; Wallace et al., 2019); flank instabilities, sector collapses and landslides (e.g., Legros et al., 2000; Bernard and de Vries, 2017); and block collision and sliding in pyroclastic density currents (e.g., Grunewald et al., 2000; Schwarzkopf et al., 2001). In each scenario, the process of frictional melting is material dependent; thus, magmas with different mineralogical assemblages may have adverse effects on the style of slip and subsequent hazards generated. Differences in mineral assemblages are expected between volcanic systems, although similar differences can be observed within the same system owing to natural heterogeneities or the dynamic nature of the plumbing system. In particular, intermediate volcanic systems can naturally evolve (both continuously and discontinuously) with regards to mineralogy and crystallinity, either reflecting long-term magmatic evolution, magma recharge, or changes in final ascent conditions (e.g., Murphy et al., 2000; Scott et al., 2013). Previous studies have reported that the introduction of hydrous phases into the plumbing system, attributed to an elevated magma-water content at depth, often coincides with an increase in explosivity (e.g., Volcán de Colima, Mexico, Luhr and Carmichael, 1990; Macias et al., 2017). Thus, the question arises as to the importance of the mineral assemblage for frictional properties in volcanic systems.

A complication that arises in the generation of a frictional melt from volcanic rocks is the common presence of a glass phase (e.g., Violay et al., 2014; Lavallée et al., 2015b). Unlike crystalline phases, which must melt to generate a liquid phase, glass exhibits a thermo-kinetic barrier, known as the glass transition temperature (T_g), where the glass softens into a liquid without any significant latent heat of reaction (Dingwell and Webb, 1989). The glass transition temperature increases with

heating rate due to the timescales available for structural relaxation, which imposes important controls on fault friction (Lavallée et al., 2015b). For a degassed rhyolitic interstitial glass, common in intermediate extrusive rocks, T_g is typically < 800 °C at moderate heating rates (e.g., < 10 °C /min), which is lower than the melting points of the minerals of its crystalline equivalent. Thus, friction with low heating rates will enable viscous remobilisation of glass at temperatures far lower than mineral melting temperatures, and therefore earlier than mineral melting itself (e.g., Lavallée et al., 2015b). However, during rapid frictional heating, T_g may be encountered at higher temperatures (e.g., ~ 1000 °C; Lavallée et al., 2015b) and closer to that of crystal melting temperatures.

Here, we experimentally assess the impact of mineralogy during the frictional melting of intermediate volcanic lavas on the evolutionary dynamics of slip. We highlight the importance of bulk mineralogy on fault properties during shallow-conduit and post-eruptive volcanic processes in high-viscosity systems (e.g., lava domes), which are as yet unaccounted for in current hazard models. A better understanding of frictional melts in systems with contrasting mineralogical assemblages will improve models for fault slip rheology and magma flow in the conduit, which in turn will aid forecasts of magma behaviour during ascent and the interpretation of early warning geophysical signals. It may also elucidate fault propagation processes at the base of rapid granular flows and help constrain run-out distances during such hazardous events.

2. Materials and methods

2.1. Starting material

Three crystal-rich, glass-bearing, intermediate dome lavas from well-characterised, active volcanic systems were chosen for this study: (1) an amphibole-bearing andesite from Soufrière Hills Volcano (SHV), Montserrat; (2) an amphibole-poor dacite from the Santiaguito dome complex (SG), Guatemala; and (3) an amphibole-free andesite from Volcán de Colima (COL), Mexico. Both SHV and COL andesites were collected from dome collapse deposits, while the SG dacite formed part of a lava spine extruded from the El Monje vent. The starting materials were chosen because they are from active volcanic systems renowned for rheological and structural instability, and because they cover a range of mineral assemblages found in intermediate lavas (andesite–dacite).

The whole-rock geochemistry of each rock sample was determined by X-ray Fluorescence Spectrometry (XRF) on a PANalytical Axios Advanced XRF spectrometer at the University of Leicester. Major elements were measured on glass beads fused from ignited powders, and trace elements were measured using pressed powder pellets (Table 1). Relative precision and accuracy were better than 1.5% for major elements and 5% for trace elements based on repeat analyses of international reference materials (see Electronic Annex). Mineral abundance statistics were collected using QEMSCAN (Quantitative Evaluation of Minerals by Scanning Electron Microscope) on an automated SEM-EDS (Scanning Electron Microscope-Energy Dispersive Spectrometer) system equipped with two Bruker energy dispersive X-ray spectrometers. QEMSCAN formulates a chemical composition from the X-ray point spectra collected in a raster across a sample and then matches the chemistry to a customisable reference library containing known compositions for minerals and glasses (for more details see, e.g., Gottlieb et al., 2000). Data were collected across an entire polished, carbon-coated thin section from each starting material using a 15 kV accelerating voltage, 5 nA beam current, 10 μm step size, and dwell time sufficient to collect enough X-ray counts for accurate phase identification (defined as 1,000 X-ray counts). The resulting data were combined to produce a false-colour phase distribution map where each colour represents a compositionally discrete phase. Each coloured pixel was summed and normalised on a pore-free basis to provide a quantitative comparison of the mineral modal abundances of each starting material (Table 2). Despite precision errors from removing and reinserting the same thin section, standard deviations were better than 0.39 for all phases. QEMSCAN identification is limited to phases larger than the beam's interaction volume ($\sim 10 \mu\text{m}^3$); groundmass phases smaller than this cannot be identified individually but are assigned the composition of the surroundings (e.g., crystals less than $\sim 2 \mu\text{m}$ in diameter surrounded by glass). Consequently, groundmass mineralogy and interstitial glass were quantified separately from point counts of > 1000 points in a $200 \times 200 \mu\text{m}$ area per sample.

2.2. Experimental procedure

Frictional melting experiments were performed using a high-velocity rotary shear (HVR) apparatus at the Kochi Core Centre in Japan. Each experiment involved the preparation of two 24.98 mm diameter plane-parallel cylindrical cores with a 9 mm hollow centre, which created an ~8 mm wide annulus to minimise variations in slip rate across the contact surface. The two cores were placed into the experimental apparatus with one core being held stationary and the other rotating. The stationary sample holder was attached to a hydraulic piston that was used to apply a controlled axial stress of 1 MPa, while the other rotated at a constant (coseismic relevant) slip rate of 1 m s^{-1} . See Hirose and Shimamoto (2005) for more details of the experimental apparatus. These slip conditions were chosen because they represent realistic estimates for those reported during faulting events, such as at active lava domes (e.g., Johnson et al., 2008; Hornby et al., 2015; Lavallée et al., 2015a), while also providing an ideal timeframe for frictional melting to allow the assessment of melting progression at different stages of slip. For each of the three starting materials, a set of five experiments was performed, with experiments terminated at five different conditions: (1) the onset of melting (T_m); (2) immediately after the achievement of steady-state conditions (T_{ss}); (3) after 5 m of slip at steady-state conditions (T_5); (4) after 10 m of slip at steady-state conditions (T_{10}); and (5) after 15 m of slip at steady-state melting conditions (T_{15}). All T_{15} experiments were performed first to act as an initial gauge for the shorter slip distance experiments; however, visual monitoring was always used to identify the onset of melting. Steady-state conditions were defined as the attainment of a near-constant value of shear stress and the beginning of sample shortening. All experiments were recorded using an optical camera to track the frictional melting process and correlate it with the mechanical data. At the end of each test, the two cores were welded together by a frictional melt layer. Post-experimental samples were thin-sectioned perpendicular to the slip surface for textural and chemical analysis.

2.3. Textural & chemical characterisation

2.3.1. Scanning electron microscopy & electron probe microanalysis

Microtextural and geochemical analyses were performed on polished, carbon coated thin sections for each experiment. Textural assessment of the frictional melt zone was performed using

backscattered electron images (BSE) taken on a Philips XL30 scanning electron microscope (SEM) at the University of Liverpool, operated with a 20 kV accelerating voltage, 5 μm spot size and a 10 μm working distance.

The compositions of the different phases present in the starting material (host-rock crystals and interstitial glass), the experimentally generated frictional melt, and any non-melted crystals suspended within the melt zone were determined using a Cameca SX100 electron probe microanalyser (EPMA) at the Ludwig Maximilian University of Munich. Elemental abundances were acquired using wavelength dispersive spectrometers (WDS). Analyses on crystals were performed using a 15 kV accelerating voltage, 20 nA beam current, and a focused ($\sim 1 \mu\text{m}$) beam. For all glass measurements, a defocussed 10 μm beam was used with a 5 nA beam current. A peak count time of 10 seconds and background count times of 5 seconds were used for all elements, with Na peaks counted first to minimise alkali loss during analysis. Matrix corrections were performed using the PAP procedure (Pouchou and Pichoir, 1984). To ensure accuracy and precision eight working standards from the Smithsonian collection were utilised throughout the analysis. The full list of reference materials, their measured and known compositions, and detection limits, along with the standards used for calibration of the spectrometers, can be found in the Electronic Annex. All standards were measured regularly to ensure quality. Reproducibility of all elements in the working standards was high, with standard deviations < 0.5 . By comparing the measured quantities with the known reference values for each standard, relative accuracies were generally better than 3% for major elements and 20% for minor elements based on multiple repeat analyses. Frictional melt compositions were measured as single points and transects across the width of the slip zone, making sure to avoid remnant crystals. Any melt totals outside 97–102 wt.% were cross-checked with BSE images and discarded in case of beam interaction with crystal fragments.

2.3.2. Synchrotron X-ray spectroscopy

Prior to EPMA, selected major and trace elements of the frictional melt were analysed by high-brightness, micron-scale X-ray spectroscopy using the I18 microfocus spectroscopy beamline at

the Diamond Light Source synchrotron, UK. Element maps were produced with a $4 \times 3 \mu\text{m}$ spatial resolution allowing detailed investigation of the extent of frictional melt homogeneity and to investigate mineral susceptibility to contribute to the melt composition. A solid-state detector system enabled the analysis of nine elements per map, of which the focus was on the concentrations of Ca, Fe, K, Ti, Mn, Rb, Sr, Y, and Zr. These elements were chosen because of their different diffusion coefficients and different concentrations in the phases (i.e., minerals and glass), making their distinction straightforward.

2.4. Frictional melt rheology

The non-Arrhenian Newtonian temperature-dependence of frictional melt viscosity was estimated using the GRD viscosity model (Giordano et al., 2008). For the viscosity-temperature model, frictional melt compositions obtained by EMPA were imported into the calculator, along with a 0.1 wt.% H_2O and zero fluorine content. These latter values were assumed based on the low water contents expected upon eruption, plus the absence of hydrous phases in the SG dacite and COL andesite (Harford et al., 2003; Reubi and Blundy, 2008; Savov et al., 2008). However, the presence of hydrous amphibole in the SHV andesite makes water content during frictional melting a variable, in addition to fluorine, which can often substitute for hydroxyl (OH^-). Although fluorine concentration in SHV amphiboles is reportedly low (0.04–0.06 wt.%; Humphreys et al., 2009), it was demonstrated that this element has a similar viscosity reduction effect as water with the tendency to remain dissolved within the melt for longer (Giordano et al., 2004). Thus, for simplicity, we assessed the impact of H_2O content on SHV frictional melt viscosity.

Apparent viscosities for the frictional melts were calculated using the recorded mechanical data from the experiments as:

$$\eta_{app} = \frac{\tau}{\dot{\epsilon}} \quad (1)$$

where τ is the recorded shear stress (in Pa) taken when slip behaviour reached a steady-state condition (i.e., shear stress attained a quasi-constant value), and $\dot{\epsilon}$ is the strain-rate (in s^{-1}). Strain-rates ($\dot{\epsilon}$) were calculated as:

$$\dot{\epsilon} = \frac{2\pi D_e}{dt} \quad (2)$$

where D_e is the circumference of the circular trajectory at a given radius (referred to as an equivalent diameter), d is assumed to reflect the thickness of the melt zone (in mm) as measured by optical analysis, and t is slip duration (in seconds). The D_e was calculated as:

$$D_e = \frac{V_e}{R\pi} \quad (3)$$

where R is the rotation rate (in min^{-1}) and V_e is the equivalent rotation velocity (i.e., displacement rate; in mm per min^{-1}). The V_e is defined as such that $\tau V_e S$ gives the rate of total frictional work on a fault with area S , assuming a constant shear stress on the fault surface after Shimamoto and Tsutsumi (1994):

$$V_e = \frac{4\pi R(D_o^2 + D_i D_o + D_i^2)}{3D_o + D_i} \quad (4)$$

where D_o and D_i are the outer and inner diameters (in mm), respectively, of the hollow core sample.

Crystals that remain in the frictional melt may also influence melt viscosity (e.g., Caricchi et al., 2007). This effect was estimated using the empirical relative-viscosity calculator of Costa et al. (2009) based on a strain-rate dependence rheology model combined with fitting parameters solved experimentally by Caricchi et al. (2007). For input values, a maximum packing fraction of 0.55 was used based on the semi-equant crystal population (Mueller et al., 2011) and a crystal fraction estimated from ImageJ (Schneider et al., 2012) using BSE images of the frictional melt. The relative effect of crystals was added to the calculated temperature-dependence of viscosity for the homogenised frictional melts to produce a modelled apparent viscosity of the suspension.

3. Results

3.1. Characterisation of the starting material

All three starting materials were crystal-rich, porphyritic, and compositionally intermediate lavas (Fig. 1; Table 1; Table 2). The sample from Soufrière Hills Volcano (SHV) was andesitic (59.6 wt.% SiO_2 ; Fig. 1a, b) and consisted of large phenocrysts of calcic-amphibole (i.e., hornblende; 9 vol.%; up to 6 mm), plagioclase (38 vol.%; up to 2 mm), orthopyroxene (5 vol.%; up to 2.5 mm), and

minor clinopyroxene, quartz, and Fe-Ti oxides. The groundmass (Fig. 1d) was highly crystalline and consisted of plagioclase (27 vol.%), pyroxene (17 vol.%), and minor Fe-Ti oxide microlites (3 vol.%). Silica-rich phases (~5 μm diameter), with characteristic fish-scale cracks (likely cristobalite, a typical byproduct of glass devitrification in SHV lavas; e.g., Horwell et al., 2013), formed the second most abundant groundmass phase (23 vol.%), while an interstitial rhyolitic glass was located between the microlite phases (19 vol.%).

The sample from the Santiaguito dome complex (SG) was dacitic (64.4 wt.% SiO_2 ; Fig. 1d, e) and had a similar porphyritic texture (phenocryst size and shape) to that of the SHV andesite (39 vol.% plagioclase and 3 vol.% orthopyroxene); however, amphibole was rare (~1 vol.%). Again, plagioclase microlites dominated the groundmass (39 vol.%; Fig. 1f), along with less abundant pyroxene (3 vol.%), Fe-Ti oxides (~1 vol.%), and a silica-rich phase (~10 μm diameter; likely tridymite, as reported for early Santiaguito lavas; e.g., Rose, 1972). These microlites were situated within an unaltered and abundant interstitial rhyolitic glass (46 vol.%).

The sample from Volcán de Colima (COL) was andesitic (62.1 wt.% SiO_2 ; Fig. 1g, h) and consisted of plagioclase phenocrysts that were more abundant (47 vol.%) and tabular (length up to 3 mm) than those in the SHV and SG samples. Both orthopyroxene (6 vol.%) and clinopyroxene (2 vol.%) were present as phenocryst phases (both up to 800 μm), in addition to rare quartz and Fe-Ti oxides. Rare, single olivine crystals were also present in the COL andesite, but owing to their infrequent appearance they were unlikely to influence frictional melting processes. Plagioclase dominated the groundmass mineralogy (30 vol.%; Fig. 1i) along with a pristine interstitial rhyolitic glass (62 vol.%), and minor pyroxene (4 vol.%) and Fe-Ti oxides (2 vol.%). Minor silica phases (2 vol.%) were occasionally located at the edges of plagioclase microlites.

3.2. Mechanical behaviour of high-velocity frictional melts

During HVR experiments, frictional melts formed on the slip plane surfaces (Fig. 2a). The slip properties of the three sample sets evolved differently (Fig. 2b); mechanical data for all experiments are displayed in the Electronic Annex (Fig. A1–A3). The frictional properties of the SHV andesite were characterised by a sudden increase in shear stress within the first metre of slip. As slip

progressed, the shear stress plateaued at 0.50 MPa for ~2 m before it strengthened to a maximum stress of 1.34 MPa at ~10 m of total slip, which coincided with incandescence along the fault contact. This was followed by the growth of melt patches, which eventually coalesced to form a molten zone that extended across the entire slip plane (T_m). Upon the formation of a continuous melt layer (at ~10 m of total slip), the SHV andesite exhibited a weakening phase that resulted in a decay of the shear stress of 0.46 MPa (from 1.34 MPa to 0.88 MPa). Further slip was characterised by the shear stress sustaining a steady-state value of 0.88 MPa until the experiment was stopped (from T_{ss} to T_{15}). Concurrent with steady-state conditions, continuous axial shortening of the sample at a constant rate of 0.12 mm/s (or 7.2 mm/m) was recorded and resulted in a total shortening of 1.4 mm after T_{15} .

The COL andesite and SG dacite showed similar frictional behaviours, despite their differences in bulk-rock composition, and contrasted with the behaviour of the SHV andesite. Both samples displayed an abrupt increase in shear stress during the first few metres of slip, which plateaued at ~0.50 MPa. Shear stress then oscillated around this value for ~9 m before strengthening to a maximum (1.83 MPa for SG and 2.00 MPa for COL) at ~15 m of total slip. Simultaneously, incandescence initiated and melt patches grew, approximately 5 m later than with SHV andesite, which eventually connected to form a single melt layer at ~12 m of total slip (T_m). With increased slip distance (> 15 m), both SG and COL samples experienced only minor shear-weakening (0.13 and 0.29 MPa, respectively) and remained at a similar steady-state condition of ~1.70 MPa from T_{ss} to T_{15} . Steady-state frictional melting was accompanied by continuous axial shortening at a rate of 0.45 mm/s (or 27 mm/min) for both SG and COL samples, almost four times faster than for the SHV andesite, which resulted in a total shortening of 5.3 and 5.5 mm after T_{15} , respectively. For all experiments, the distance and time to the onset of melting varied owing to natural heterogeneities in the lava samples (Fig. 2c; Fig. A1–A3); thus, for textural and chemical analysis, each frictional melt was normalised with respect to the onset of melting (i.e., $T_m = 0$ m and 0 s) to allow direct comparison across sample sets.

3.3. Microtextural evolution

SHV andesite produced the thinnest melt zones (0.1–0.4 mm thick), while SG dacite and COL andesite generated thicker frictional melts (0.2–1.0 mm thick). At the onset of melting (T_m), the frictional melts exhibited ultra-fine broken crystals ($< 5 \mu\text{m}$) suspended within a melt that quenched to a glass after the experiment was stopped (Fig. 3). These crystal fragments were mineralogically the same as those recorded in the host-rock, except for amphibole, an abundant phase in the SHV andesite, which was not found as a remnant crystal within the entire melt zone. BSE images of the melt zones at T_m showed subtle grey-scale heterogeneities in the frictional melt phase (Fig. 3). For frictional melts that reached steady-state (T_{ss}), the number of finely suspended clasts had reduced while the melt fraction had increased (Fig. 3). Larger crystal fragments (up to $40 \mu\text{m}$ in diameter), primarily plagioclase, also became more isolated within the melt. From 5 m of steady-state slip onwards (T_5 – T_{15}), all frictional melt zones contained large (up to $80 \mu\text{m}$) relic plagioclase fragments that were equant with rounded edges. Partially resorbed rims around these fragments were also a characteristic feature (Fig. 3 T_{10} and T_{15}). Furthermore, the silica-rich phases observed in the host groundmass of the SHV andesite and SG dacite appear undisturbed in the frictional melts, with their original shape and surficial textures remaining unaltered.

All melt layers contained circular and evenly distributed micro-bubbles, although their sizes and number densities were dependent on the host material involved. The SHV melts displayed consistently large and abundant bubbles that increased in size with slip distance (from < 5 to $14 \mu\text{m}$ diameter). SG and COL melts showed fewer and smaller bubbles ($< 5 \mu\text{m}$ diameter) with little systematic variation with slip distance. The irregular voids observed in the melt zones (Fig. 3) likely reflect an artefact of plucked crystals due to sample polishing and should not be mistaken for vesicles.

3.4. Frictional melt compositional variability

The SiO_2 concentration in the SHV frictional melts ranged from 54.5 wt.% to 72.3 wt.% (Fig. 4a), while the compositions of the SG (Fig. 4b) and COL (Fig. 4c) frictional melts were more restricted (60.3–72.4 wt.% and 59.5–66.6 wt.%, respectively). Similarly, the ranges in MgO and FeO were 3–4 times larger in the SHV melts compared with the SG and COL melts. For all frictional

melts, their composition evolved as slip distance increased, although the style of chemical progression showed a dependence on the starting material. For both the SG and COL melts, as slip distance increased from T_m to T_{15} , the variability in melt composition decreased and eventually approached a near-homogeneous equivalent to its bulk-rock composition. Discrepancies between melt composition and the bulk-rock composition were expected, owing to incomplete melting of crystalline fragments (Fig. 3). In contrast, the SHV melts became increasingly mafic with time, as reflected by a progressive increase in FeO and MgO. Although compositional discrepancies existed for all frictional melts, binary plots defined a quasi-linear pattern depending on the element oxide (Fig. 4). Some element oxide pairs displayed a strong linear relationship (e.g., SHV FeO vs. MgO, SG SiO₂ vs. Al₂O₃), with compositions located along a classic mixing line between host-rock plagioclase and interstitial glass, while others showed a larger degree of variability away from this trend (e.g., SHV SiO₂ vs. Al₂O₃, SHV and SG Al₂O₃ vs. Na₂O). Transects perpendicular to the melt zone were also analysed for compositional variability (Fig. A4). These transects recorded a similar trend to that observed in the binary plots, although the higher spatial resolution provided more detail of the extent of melt heterogeneity within a localised area and how it evolved with slip distance. All chemical transects revealed homogenisation towards the bulk-rock composition from T_m to T_{15} . However, only in the SHV melt zones that went beyond T_{ss} did the melt composition deviate from that of the bulk-rock, while SG and COL melts maintained a composition close to the precursor material.

Evaluating compositional variations through time required careful consideration of all the different components present within the system, as their diffusivities can vary greatly. The standard deviations of concentration across the melt zone for each major element oxide showed an exponential decrease with slip distance (Fig. 5). For each starting material, a similar systematic ordering of the decay curves was observed, with SiO₂ and Al₂O₃ showing the largest variability (Fig. 5a, b). This ordering roughly correlated to relative diffusivities of the measured components. The melt derived from the SHV andesite showed the largest standard deviations throughout, with the most homogenous melt compositions at T_{15} being comparable to those at T_m for SG dacite and COL andesite (Fig. 5a–f).

3.5. Crystal-melt interaction

Areas of interest for electron probe microanalysis (EPMA) and high-resolution synchrotron X-ray spectroscopy were selected, where each phase was in direct contact with the melt zone, to investigate its susceptibility to breakdown and incorporation in the melt zone. Where amphibole crystals were found adjacent to the SHV melt zone, the frictional melt was often twice as thick as anywhere else along the slip plane (Fig. 6a). Texturally, amphibole-melt contacts were transitional (Fig. 6b), exhibiting: (1) an intact amphibole phenocryst; (2) a partially embayed amphibole, with increased embayment towards the melt zone; and (3) a fully formed frictional melt zone. An EPMA transect across this contact region revealed the direct transfer of amphibole components to the melt, which resulted in a quasi-linear gradational trend for major components (Fig. 6c). Components that are low in concentration in amphiboles (e.g., Na_2O) showed only minor influence on melt composition. Element maps along the amphibole-melt contact also depicted the contribution of key elements to frictional melt composition (Fig. 6d and Fig. A5); in particular, the adjacent melts were enriched with Ca, Fe, and Y, along with minor Ti and Mn. Although K, Sr, Rb, and Zr are incompatible in amphibole, they were still detected in the melt. Fe-Ti oxide crystals in the melt zones appeared less affected by the high temperatures, although they often showed a subtle halo of Ti-rich melt (Fig. 6d).

In contrast to the amphibole-melt relationship, when plagioclase phenocrysts were in contact with the melt zones no embayment textures were observed (Fig. 6a); in these areas, the melt layers were often the thinnest ($< 50 \mu\text{m}$; Fig. A6). Plagioclase is similarly abundant in Ca as other phases in the host materials (e.g., amphibole and clinopyroxene), yet its high Sr compatibility allows easy detection and makes its involvement in frictional melt composition distinct. X-ray spectroscopy maps revealed that SG and COL frictional melts were all notably enriched in Sr (Fig. 7 and A7), although the SHV melts were all relatively Sr poor (Fig. 6, A5 and A6). Augite (clinopyroxene) and hypersthene (orthopyroxene) were the dominant pyroxene phases in all three host materials (see Electronic Annex). Although pyroxenes are generally similar in composition to amphiboles, they are importantly anhydrous and lacked resorption textures when in contact with the melt zone (Fig. A6 and A7). In these areas, SG and COL frictional melts were noticeably lower in Ca and Fe and overall less compositionally heterogeneous compared with the SHV melts. Within the SG and COL melts, the

contribution of interstitial glass was identified by the high concentration of K, along with zones that showed elevated concentrations of Rb and Zr (Fig. 7 and A7). However, K, Rb, and Zr were low in concentration in the SHV melts (Fig. 6 and Fig. A5).

Mass balance mineral contributions to each frictional melt composition were calculated by applying the adapted least squares petrological mixing program MINSQ (Herrmann and Berry, 2002), using the compositions of host-rock minerals, interstitial glass, and frictional melts from EPMA. Given that the chemical compositions of these phases were expressed as weight percentage of element oxides, modal phase proportions were also calculated as weight percentages. Weight percentages were converted to volume percentages for comparison with measured abundances in the host-rock using the following phase densities (g cm^{-3}): amphibole = 3.2, plagioclase = 2.7, clinopyroxene = 3.3, orthopyroxene = 3.5, Fe-oxide = 5.2, quartz (for Si-phases) = 2.6 and glass = 2.4. In the least squares calculations, frictional melt compositions from each experiment were used as the target composition and the host-rock minerals and interstitial glass as the contributing phases. Figure 8 shows the major contributing phases for the entire range of compositions measured in each sample suite and how their abundance evolved with slip distance. From these results, calcic-amphibole (hornblende) was shown to be a key component of the SHV melt composition, with the measured melts estimated to have a 0–27 vol.% amphibole contribution (Fig. 8a). At the early stages of melting (T_m-T_{ss}), an average of 6–7 vol.% amphibole was estimated to contribute to the frictional melt composition, but after steady-state melting was achieved, up to 27 vol.% amphibole was incorporated into the melt, consistent with the evolution observed in the binary plots (Fig. 4a). Plagioclase dominated the frictional melt modal compositions in all samples (Fig. 8b), albeit underrepresented relative to the bulk mineralogy. There was a general decrease in plagioclase abundance and variability with slip distance, which averaged between 43 and 50 vol.% at T_{15} for each starting material. Interstitial glass was the second-most influential phase on melt composition, which appeared to be overrepresented relative to the bulk-rock (Fig. 8c). Similar to plagioclase, the contribution range of interstitial glass to melt composition became less variable with slip distance; however, the evolutionary trends between the three sample sets were different. SHV melts showed an average decrease in glass contribution with slip distance (from 43 to 35 vol.%), while the proportions of glass in both SG and COL melts increased (from 31 to

44 vol.% and 31 to 36 vol.%, respectively). All frictional melts showed an increase in orthopyroxene (hypersthene) melting with slip distance (Fig. 8d), although SG and COL melts were underrepresented compared with the bulk. Clinopyroxene (augite) had only a minor involvement in the compositions of the SHV and SG melts; however, the COL melts showed a more significant clinopyroxene contribution (Fig. 8e), consistent with its occurrence as large phenocrysts in the COL andesite. Fe-Ti oxides represented a minor component of all melt compositions, yet still revealed a subtle increase with slip distance (Fig. 8f).

The same least squares model was employed to approximate a theoretical proportion of phases required to further melt and incorporate with the frictional melts to obtain the bulk-rock composition. The measured fraction of homogenised frictional melt (quantified using BSE images) was combined with the compositions of crystal fragments remaining in the melt zone to obtain the following:

$$1 \text{ SHV Bulk} = 0.53 \text{ Melt} + 0.33 \text{ plag} + 0.05 \text{ glass matrix} + 0.06 \text{ qtz} + 0.02 \text{ Ti mag} + 0.02 \text{ opx(Hyp)} \pm \text{cpx(Aug)} \quad (5)$$

$$1 \text{ COL Bulk} = 0.65 \text{ Melt} + 0.24 \text{ plag} + 0.08 \text{ qtz} + 0.01 \text{ Ti mag} + 0.02 \text{ opx(Hyp)} \pm \text{cpx(Aug)} \quad (6)$$

$$1 \text{ SG Bulk} = 0.53 \text{ Melt} + 0.29 \text{ plag} + 0.13 \text{ qtz} + 0.03 \text{ Ti mag} + 0.02 \text{ opx(Hyp)} \pm \text{cpx(Aug)} \quad (7)$$

These estimated phase proportions were consistent with observations seen in BSE images of the melt zone at T_{15} (Fig. 3).

3.6. Rheological response of frictional melt

Silicate melt viscosity is primarily determined by chemical composition. Frictional melt viscosities were estimated using the empirical equation of Giordano et al. (2008). Owing to the large compositional heterogeneities for melts formed between T_m and T_{ss} , obtaining a single value for melt viscosity for these melts is challenging. However, the more homogenous melt compositions at T_{15} formed the closest to an equilibrium state, which permitted a more robust approximation for the temperature-dependence of viscosity.

Figure 9a–c displays the temperature-viscosity relationships for the homogenised frictional melts for each starting material, plus felsic and mafic melt filaments formed at the onset of melting which act as viscosity end-members. For comparison, viscosities were also calculated for the

interstitial glass and molten bulk-rock. The relative effect of solid particles suspended in the melt (estimated using Costa et al., 2009) was added to the temperature-dependence of melt viscosity derived from Giordano et al. (2008) to model its apparent viscosity. For the homogenised frictional melts at T_{15} derived from SHV, COL, and SG samples, the presence of crystals added 0.92, 0.63, and 0.36 orders of magnitude of [Pa s] to the viscosity, respectively (Table 3). Through calculating an apparent viscosity derived from the mechanical data (Eq. 1) and comparing these values to the modelled temperature-dependent viscosity curves for each sample (Fig. 9a–c), estimates of the temperature range for the frictional melts during steady-state slip were obtained. The SHV melts had an estimated viscosity range of 1.95–2.17 [log Pa s] across a wide temperature range from 1270 °C (for a crystal-free melt) to 1510 °C (if the melt contained up to 45 vol.% crystal suspensions; Table 3). SG and COL melts revealed overlapping viscosity ranges (of 2.33–2.54 and 2.41–2.73 [log Pa s], respectively), which were consistently higher than the SHV melts. However, estimated temperatures for both SG and COL melts differed significantly from 1400 °C to 1510 °C and 1280 °C to 1440 °C, respectively. It is important to note that these viscosities, and thus temperature ranges, could be a slight overestimate owing to the possible underestimation of the melt zone thickness (as required for strain-rate calculations; Eq. 2). Figure 9d shows the effect of increasing water content on the temperature-dependent modelled apparent viscosity of the homogenised SHV frictional melt suspension. It demonstrates that if the SHV melts contained water, the modelled apparent viscosities would be lower; thus, the SHV melt zones would require a lower temperature to achieve the apparent viscosities measured using the mechanical data (Eq. 1).

4. Discussion

4.1. Mechanisms driving frictional melting of volcanic rocks

Amongst the many studies that exist on tribological instabilities, dynamic fault slip events are typically described using a rate- and state-dependent friction law (e.g., Dieterich, 1979; Rice et al., 2001; Ohmura and Kawamura, 2007; Popov et al., 2012). Previous experimental investigations on the frictional properties of igneous, metamorphic, and sedimentary rocks have highlighted their dynamic evolution with increasing displacement, a consequence of thermal instabilities brought about by

frictional heating and subsequent melting (e.g., Tsutsumi and Shimamoto, 1997; Hirose and Shimamoto, 2005; Di Toro et al., 2011; Niemeijer et al., 2011; Chen et al., 2017; Lockner et al., 2017). Furthermore, the frictional behaviour of both intrusive and extrusive igneous rocks at coseismic slip rates ($> 0.1 \text{ m s}^{-1}$) has been shown to inherit complex transient regimes in the form of both shear-weakening and strengthening (e.g., Tsutsumi and Shimamoto, 1997; Hirose and Shimamoto, 2005; Kendrick et al., 2014b; Hornby et al., 2015; Chen et al., 2017). Analogous to these reports, the frictional behaviour of the three mineralogically contrasting lavas in the present study can be divided into three discrete stages: (1) an initial steady-state regime; (2) a shear-strengthening regime; and (3) a final shear-weakening to steady-state slip regime. The timing and intensity of each of these stages was material dependent. The SHV andesite experienced only a minor stage 1, lasting just 1–2 m of slip, whereas SG dacite and COL andesite spent ~ 10 m at this stage. The transition to stage 2 was similar in all cases, although SG and COL samples continued to strengthen to a higher peak stress and underwent only minor shear weakening during stage 3. In contrast, the SHV andesite reached a lower shear stress and experienced a more distinct shear-weakening step during stage 3. These observations were similar to previous studies of volcanic rocks, with their differences in slip properties attributed to a contrast in mineral assemblage and the presence of an interstitial glass (Kendrick et al., 2014b). The work of Spray (1992) highlighted the significance of a host material's constituent minerals on frictional properties. Accordingly, a hierarchy of frictional melting susceptibility for a range of common rock-forming minerals was constructed, taking into account their shear strength, fracture toughness and most importantly melting point. Applying this hierarchy to the individual phases of the three lavas in this study, the theoretical order of phases preferentially affected during frictional sliding would be rhyolitic glass ($T_g = 740\text{--}770 \text{ }^\circ\text{C}$, estimated using Giordano et al. (2008) as a viscosity gauge for 10^{12} Pa s ; Fig. 9a–c), calcic-amphibole (hornblende; $\sim 750\text{--}1000 \text{ }^\circ\text{C}$), plagioclase ($\text{An}_{40}\text{--}\text{An}_{90}$; $\sim 1280\text{--}1500 \text{ }^\circ\text{C}$), clinopyroxene (augite; $\sim 1400 \text{ }^\circ\text{C}$), orthopyroxene (hypersthene; $\sim 1425 \text{ }^\circ\text{C}$), Fe-Ti oxides ($\sim 1600 \text{ }^\circ\text{C}$), and Si-polymorphs (SiO_2 ; $\sim 1700 \text{ }^\circ\text{C}$). However, due to the fast heating rates involved during frictional heating and melting, the T_g for the rhyolitic interstitial glass may be higher than the melting temperature of amphibole.

The marked increase in shear stress at the onset of friction is attributed to the initial interaction of asperities on the slip surfaces, which led to subsequent comminution of the host-rock and likely coincided with minor plucking of minerals. In the SHV andesite, amphibole was the mineral most susceptible to grain size reduction owing to its lower fracture toughness and yield strength (Spray, 1992); for SG and COL samples, the mechanically weakest mineral was plagioclase (Spray, 1992). Additionally, the high abundance of silica phases in the groundmass of the SHV andesite (due to glass devitrification) likely had more of a physical effect at the early stages of slip than an unaltered glass. This micromechanical response resulted in the formation of a cataclastic gouge layer on the contact surface (e.g., Hetzel et al., 1996; Spagnuolo et al., 2016), which acted as a lubricant and permitted minor shear weakening that led to near steady-state shear stress within the first few metres of slip (e.g., Reches and Lockner, 2010; Lavallée et al., 2014). Frictional heating caused an abrupt shear strengthening attributed to volumetric expansion of the sample (as seen in the shortening data; Fig. 2b) and the first production of a melt on the slip plane. The preferential melting of ultra-fine crystal fragments, owing to their larger surface area (Spray, 1992), generated molten patches on the slip surface (Tsutsumi and Shimamoto, 1997; Hirose and Shimamoto, 2005; Chen et al., 2017). These melt patches behaved as a preliminary viscous brake and caused the shear stress to rise to a maximum (Tsutsumi and Shimamoto, 1997; Fialko and Khazan, 2005; Hirose and Shimamoto, 2005). Owing to the ubiquitous occurrence of amphibole in the SHV andesite, this process took place ~5 m (5 s) earlier than in the experiments with the SG dacite and COL andesite. This shorter slip distance required to generate melt could be related to a higher rate of comminution followed by the preferential melting of the amphibole fraction. It has also been postulated that the release of water from the melting of hydrous phases could facilitate this stage (e.g., Allen, 1979; Hetzel et al., 1996). As the temperature increased concurrently with shear stress, melt patches began to coalesce upon increased melting, resulting in a molten layer with abundant crystal fragments, as seen at the onset of melting (T_m ; Fig. 3). With further melting, a fully formed frictional melt separated the two sliding surfaces, owing to an increase in the volume of melt to crystals, until a critical melt fraction is reached (Fialko and Khazan, 2005; Rosenberg and Handy, 2005; Chen et al., 2017). Thickening of the molten layer accompanied by increased melting caused a decrease in shear stress

towards a steady-state condition (e.g., Tsutsumi and Shimamoto, 1997), which increased the distance between the two opposing interfaces (referred to as the Stefan problem; e.g., Hirose and Shimamoto, 2005). At this stage, slip behaviour was dependent on the viscosity of the melt, which in turn was influenced by the strain-rate in the slip zone. The SHV andesite showed a larger shear weakening response (0.46 MPa) compared with SG dacite (0.13 MPa) and COL andesite (0.29 MPa), which matched the variation in estimated frictional melt viscosities for each material (Fig. 9; Table 3). From this stage on, the ability of the slip zone to sustain a molten layer was determined by the heat produced by shear heating rather than solid friction (Hirose and Shimamoto, 2005). Microstructural evidence of a reduction in finer crystal fragments upon steady-state melting confirmed this (Fig. 3), suggesting that intense comminution was no longer in action. Steady-state conditions were marked by a sudden increase in melt production as maximum temperatures were reached. Here, comminution was replaced by tearing of crystals along the slip interface. Consequently, large angular crystal fragments, derived from the host material, became isolated within the molten layer (from T_{ss} onwards; Fig. 3) and their outer edges subsequently became rounded owing to combined attrition and melting (Lin, 1999), a characteristic feature of natural pseudotachylytes (e.g., Sibson, 1975). Melting of the outer edges of plagioclase fragments generated the resorbed rim textures (Fig. 3), which demonstrated that these fragments were subjected to temperatures exceeding their equilibrium conditions. The thickening of the melt zone and change in shape of the rock-melt interface towards steady-state conditions was an important characteristic that likely altered the roughness of the fault plane and affected the frictional properties (i.e., flow rheology). Such a change in melt-surface topography was most noticeably brought about by the interaction of amphibole crystals with the melt zone (Fig. 6a). Amphibole embayment along with a consistently thicker melt zone adjacent to amphibole crystals provided evidence for its selective melting (e.g., Spray, 1992). Similar textures have been related to the Gibbs-Thomson effect (Hirose and Shimamoto, 2003), by which the local melting temperature of a mineral's external surface—when in contact with the melt zone—is reduced. In contrast, plagioclase crystals showed less textural evidence for melting, which corresponds to a thinner melt layer when plagioclase phenocrysts are adjacent to the slip zone (Fig. 6 and Fig. A6). The variation in final melt thickness between each sample set corresponded to the amount of shortening experienced during the

experimental run (Fig. 2b). However, it is possible that the melt thickness measured may not be fully representative because the melt zone may have been compressed slightly after the experiment ceased, while a normal stress (1 MPa) was still being applied.

4.2. Selective phase melting and preferential melting of amphibole

Frictional melting has long been portrayed as a disequilibrium selective mineral melting process (Shimamoto and Lin, 1994; Lin and Shimamoto, 1998), yet the influence of discrete phases on the mechanics of frictional melt production during faulting remains an area that is not fully constrained (e.g., Jiang et al., 2015). Here, we relate mechanical and compositional progression of frictional melting to the presence or absence of amphibole in the host material. Although interstitial glass was more abundant in the SG dacite and COL andesite than in the SHV andesite, it was likely to have a secondary role on the mechanical properties when amphibole was present; this may be a consequence of the high heating rates involved, limiting the timescale of structural relaxation of the glass, and possibly resulted in T_g being higher than the melting point of amphibole (e.g., Dingwell and Webb, 1989; Lavallée et al., 2015b). Previous HVR experiments on the frictional melting of andesites and dacites that were both glass-rich and amphibole-rich (e.g., Kendrick et al., 2014b; Hornby et al., 2015) recorded similar mechanical behaviours to the SHV andesite in this study, supporting the theory that hydrous minerals have a primary control on frictional behaviour. The absence of amphibole fragments hosted within the SHV frictional melt supports the disequilibrium melting model of Spray (1992), where amphibole has the lowest melting point; other studies also reported the lack of ferromagnesian hydrous fragments in experimental melts and natural pseudotachylytes (e.g., Scott and Drever, 1953; Sibson, 1975; Hetzel et al., 1996; Hirose and Shimamoto, 2005; Jiang et al., 2015). The composition of the melts can thus be related to the chemical components that were derived from melting of the different host-rock phases, as revealed by the least squares model (Fig. 8).

All melt compositions showed a near-linear relationship between the composition of the interstitial glass and plagioclase (Fig. 4), suggesting that these two phases were influential in the melting process. However, a deviation from this trend may have come from either a combination of contrasting mobilities of different chemical elements, referred to as diffusive fractionation (e.g.,

Perugini et al., 2006; Morgavi et al., 2013; Perugini et al., 2013), or the interaction of mafic minerals (e.g., amphiboles, pyroxenes, and Fe-Ti oxides). The high level of Sr in the SG and COL frictional melts confirms the dominance of plagioclase melting. Additionally, the elevated K, Rb, and Zr in these melts demonstrates melting of the interstitial glass was integral during frictional melting of SG dacite and COL andesite; this is consistent with the higher abundance of K-rich interstitial glass in their host material. A low concentration of K, Sr, Rb, and Zr in the SHV frictional melts suggests melting of plagioclase and glass was more limited, consistent with less interstitial glass in the host material, as the preferential melting of amphibole proceeded. Interestingly, the compositions of the SHV melt at the onset of melting showed only minor amphibole influence based on lower ferromagnesian components (Fig. 4); this is supported by the least squares model (Fig. 8a). This lack of amphibole contribution was likely due to the absence of amphibole phenocrysts adjacent to or on the slip plane. With slip progression, an overall increase in FeO, MgO, and CaO, along with a slight decrease in Al₂O₃, suggests an increased amphibole contribution, which also corresponds to the increase in bubble content. Homogenisation towards the host's bulk composition, which has been proposed previously (e.g., Spray, 1992; Hirose and Shimamoto, 2005), appeared to be the case upon steady-state melting (T_{ss}) due to increased mixing efficiency. However, owing to preferential amphibole melting in the SHV andesite, the melt composition became more mafic with time. This contrasts with the interpretation of Jiang et al. (2015), who suggested that melts will become progressively more felsic with time if hydrous phases are present. An increased amphibole input was likely the result of the conduction of heat through the sample. High temperatures would have initiated along the fault plane, which would only allow phases exposed to the contact surface to melt (i.e., plagioclase and glass). However, as melting progressed, a strong thermal gradient between the melt zone and the host-rock surface likely formed (e.g., Nielsen et al., 2008). Consequently, any heat being transferred through the host's wall may have been limited to a small distance from the interface where temperatures may not have been high enough to melt most minerals that were directly adjacent to the melt zone. However, owing to amphiboles having a significantly lower melting temperature compared with the other phases (750–1000 °C; Spray, 1992), these minerals were likely still affected even if temperatures were several hundreds of degrees lower than in the melt zone interior. The textures

observed in Figure 6b confirm this, where amphibole began to melt ~200 μm away from the melt zone. A similar effect has been observed on landslide slip surfaces, in which minerals directly beneath the fault plane had thermally decomposed owing to frictional heating (Hu et al., 2018). It is also possible that mafic melt filaments that formed at the onset of melting could have been compromised owing to rapid diffusion related to low viscosities (e.g., Rossi et al., 2017), unlike more felsic filaments with higher viscosities; this may further explain the apparent lack of amphibole signature at the onset. However, the mafic trend with slip progression opens a potential case for amphibole-bearing rocks not being able to (or required to) produce frictional melt temperatures high enough for efficient bulk melting, creating a feedback that encourages mafic compositions.

Compositional trends for the SG and COL melts fit the expected evolution towards homogeneity and bulk-rock composition with increasing slip distance. Although these melts initially had a hybridised composition between plagioclase and interstitial glass, an increase in FeO and MgO with time confirms the melting of pyroxenes. The lack of a CaO trend for these melts suggests the contribution of orthopyroxene to frictional melt composition dominated over clinopyroxene, which corresponds to the relative modal fractions in the host materials. Although clinopyroxene (augite) and orthopyroxene (hypersthene) have similar estimated melting temperatures (~1400 °C and ~1425 °C, respectively), orthopyroxene generally has a lower yield strength and shear strength (Spray, 1992), which may have favoured faster comminution and subsequent melting from the onset of slip. The presence of silica phases suspended in the SHV and SG frictional melts (derived from the host's groundmass; Fig. 3) confirms the higher temperatures required to melt them (> 1700 °C). However, mass balance calculations for the SG frictional melt suggest that some melt filaments required up to 28 vol.% of a pure silica phase to obtain its composition. From the temperature-viscosity model (Fig. 9), estimated temperatures of the molten layer rarely exceeded 1500 °C. However, Lee et al. (2017) showed that the melting temperature of quartz could be suppressed by > 200 °C owing to preferential melting of finer quartz fractions and conversion to a meta-stable β -quartz, referred to as quasi-equilibrium melting.

4.3. Chaotic mixing and chemical homogenisation during frictional melting

The evolution of frictional melt composition during the progressive melting of chemically discrete phases is governed by a dynamic chaotic mixing phenomenon, akin to magma mixing (e.g., Perugini et al., 2003; De Campos et al., 2011). In recent years, chaotic mixing between mafic and felsic silicate melts has been constrained experimentally to assess the timescales of chemical homogenisation during magma mixing events (e.g., Morgavi et al., 2013; Perugini et al., 2013; Rossi et al., 2017). The diffusivities of the different major elements alone would not permit the chemical exchanges observed over the timescales of frictional melting in our experiments (< 20 s); thus, physical mixing must play a fundamental role. At the onset of melting (T_m), the formation of melt filaments within the molten layer generated compositional gradients; owing to shearing, these filaments began to stretch and fold, which increased the surface area to enhance chemical diffusion. Owing to different element diffusivities, this may have caused a diffusive fractionation resulting in melts with a hybridised composition (Perugini et al., 2006; Perugini et al., 2008; Perugini et al., 2013). In a simple case, the mixing of two melts (with one component) should form linear trends in binary plots (e.g., Fourcade and Allègre, 1981). However, owing to the fractal distribution of melt filaments and a frictional melt consisting of more than two end-members with multiple components, a non-linear trend between elements exists (Fig. 4), which highlights the complexity involved during chemical mixing of a frictional melt. Consequently, discriminating the effect of diffusive fractionation and the range of chemical filaments involved is a challenging task.

Gradational melt filaments observed in BSE images of the frictional melts (Fig. 3 T_m) likely represent local areas of immiscibility and incomplete mixing of the different melted phases (termed schlieren). The various compositions of these different filaments suggest that viscosity contrasts would exist within a frictional melt. These viscosity contrasts would have a significant influence on melt filament mixing efficiency (e.g., Sparks and Marshall, 1986), with a larger viscosity contrast taking more time to mix and homogenise (e.g., Morgavi et al., 2013). The large viscosity contrasts expected between amphibole, plagioclase, and interstitial glass filaments could explain the more heterogeneous nature of the SHV melts (Fig. 4a). The smaller viscosity contrasts between plagioclase and glass in the SG and COL melts would aid a faster rate of homogenisation (Fig. 4b, c). Owing to density variations brought about by varying chemical compositions of the melt filaments, mixing

during frictional melting can be described as a form of double-diffusion convection, where convection is forced by filaments with juxtaposing diffusivities (Huppert and Sparks, 1984; Hirose and Shimamoto, 2005). In summary, we highlight the complexity involved when attempting to assess chaotic mixing of a frictional melt due to selective phase melting.

4.4. Rheology

As discussed, the dynamic physicochemical complexity of a frictional melt brings about a convoluted rheological response. It has been well documented that the viscosity of the growing molten layer between two sliding surfaces determined the shear resistance of a melt during slip (e.g., Hirose and Shimamoto, 2005). Consequently, it is the viscosity dependence that determines whether a frictional melt will serve as a lubricant or brake (e.g., Koizumi et al., 2004; Hirose and Shimamoto, 2005; Kendrick et al., 2014b). The mafic trend observed in the SHV frictional melts suggests a likely decrease in melt viscosity with slip distance owing to increased amphibole-melt interaction. Heat transfer to the wall rock adjacent to the melt layer can result in a continuous injection of low-viscosity amphibole melt causing the viscosity to be dynamic. However, the more homogenising response of the SG and COL melts suggests a more constant viscosity with time. This response may be the cause for the instantaneous transition from peak shear stress to steady-state with little weakening involved (Fig. 2b); this was in contrast to the SHV melt, which showed a clear weakening phase before steady-state conditions were achieved.

The presence of crystals and bubbles within a frictional melt can influence the apparent viscosity (Lavallée et al., 2012; Hornby et al., 2015). Crystals in all the frictional melts increase shear resistance by adding between 0.36 and 0.97 Pa s to the apparent viscosity causing increased strain-rate dependence (Fig. 9a–c). However, bubbles may either increase apparent viscosity or have an opposite effect depending on whether the bubbles can resist deformation or deform viscously, respectively (e.g., Bagdassarov and Dingwell, 1992). As highlighted by Lavallée et al. (2012), the low estimated viscosities of the frictional melt imply that bubbles should deform, lowering the apparent viscosity. Yet, bubbles showed no signs of deformation (Fig. 3). Undeformed bubbles were previously given as evidence for their formation at the end of sliding (Hirose and Shimamoto, 2005). However, circular

bubbles more likely reflect the relaxation of a low viscosity melt that was dominated by highly isotropic surface tension which bring the bubbles back to spherical once shearing has ceased (Rust and Manga, 2002). The increase in bubble content with slip distance in the SHV melt is attributed to elevated water contents due to increasing input from amphibole melt. With amphibole containing ~2 wt.% H₂O in its structure, a contribution of 27 vol.% amphibole melt (Fig. 8a) may have resulted in up to 0.54 wt.% H₂O being transferred to the frictional melt, and thus lowered the modelled apparent viscosity and lowered the estimated temperatures of the SHV melt zone by ~100 °C (Fig. 9d).

The apparent viscosity of the frictional melt suspension is strain-rate dependent and results in dynamic slip mechanics. In nature, slip rates are rarely constant. Based on the non-Newtonian nature of silicate melts (e.g., Webb and Dingwell, 1990), a decrease in slip velocity would result in a reduced strain-rate causing an increase in apparent viscosity. This may manifest as a rise in shear stress that exceeds the structural relaxation of the melt causing slip to terminate. The slip zone may subsequently heal and then reactivate following the accumulation of shear stress, resulting in a stick-slip motion (e.g., Koizumi et al., 2004; Kendrick et al., 2014b; Lavallée et al., 2015b; Lockner et al., 2017). Consequently, we infer that host materials bearing a similar mineral assemblage to SG dacite and COL andesite are more likely to form frictional melts that operate as a viscous brake during deceleration of fault slip. On the other hand, in materials bearing a high abundance of hydrous minerals, similar to the SHV andesite, frictional melts would lubricate slip even during deceleration.

5. Implications for volcanic settings

During the ascent of high-temperature, high-viscosity magma, common during dome-building eruptions, strain localisation along the conduit margins can result in the development of shear zones that experience seismogenic failure as magma encounters the viscous-brittle transition (e.g., Neuberg et al., 2006; De Angelis and Henton, 2011; Kendrick et al., 2014a). High strain-rates in these regions can lead to frictional melting along the faulted contact and, consequently, dictate ascent dynamics and influence the style of activity at the surface (Kendrick et al., 2014a).

At Santiaguito dome complex (Guatemala), regular gas-and-ash explosions have been attributed to strain localisation and friction during piston-like faulting of a lava plug at the conduit

margins due to rapid uplift of the dome, corresponding to a slip velocity of up to 1 m s^{-1} (Johnson et al., 2008). Evidence of frictional melting was recorded by the presence of melt filaments in erupted ash fragments and frictional marks on blocks forming the dome carapace (Lavallée et al., 2015a). In addition to explosive activity, Hornby et al. (2015) reported that frictional melting was a likely process during repetitive slip of an emerging lava spine at Unzen volcano (Japan) following an experimental investigation. The study coupled high-velocity rotary shear experiments with seismic signals recorded during spine growth and constrained a slip velocity of 0.75 m s^{-1} . Shear zones that developed at the margins of the lava spine during its extrusion record extensive petrological evidence for localised frictional deformation and subsequent heating (Wallace et al., 2019).

The difficulty we face when identifying pseudotachylytes in volcanic conduits is the high and sustained ambient temperatures ($> 500 \text{ }^\circ\text{C}$) which promote slow cooling, crystallisation, hydrothermal alteration, and the metastability of glass. Such post-melting alteration processes can result in chemical, textural, and geophysical overprints that make it difficult to decipher the conditions of frictional melting (e.g., Kendrick et al., 2012; Kirkpatrick and Rowe, 2013).

Fluxes in the abundance of mineral phases have been observed in many volcanic systems, particularly hydrous phases that are attributed to the injection of hydrous magma. Volcán de Colima has experienced such events, where an increased abundance of amphibole was recorded in products erupted in 1818 and from 1869 to 1913. This has been labelled as a potential precursor of explosive activity (Luhr and Carmichael, 1990; Luhr, 2002; Savov et al., 2008; Saucedo et al., 2010). We suggest that the introduction of amphibole could play a fundamental role in altering flow dynamics in the upper conduit by reducing the shear resistance during slip and facilitating explosive behaviour. This is because a lubricating effect could enable a continuous, fast magma ascent in the conduit where less shear resistance takes place near conduit margins. As amphibole-derived frictional melts are less likely to act as viscous brakes during a deceleration in magma ascent rate, they may be less prone to generate permeable fractures. Additionally, our observations that lavas containing amphibole generate frictional melts faster than amphibole-free lavas suggest amphibole-bearing systems are more susceptible to frictional melting. Consequently, the rapid formation of frictional melts in amphibole-bearing systems following short slip events may help seal fault planes that subsequently heal, thus

decreasing the permeability of the system. Both these mechanisms promote higher gas overpressures and greater explosivity. If the magma is amphibole-free, frictional melts are less likely to form during very short slip events, and even during prolonged slip frictional melts are more likely to fail and fracture, leading to a pulsatory magma ascent in a stick-slip motion. Thus, frictional melting in amphibole-free systems favours the development of outgassing pathways that relieve the pressure of the system and reduce the explosive potential. However, for hydrous phases to control frictional behaviour, their abundances would likely need to be above a critical fraction to ensure continuous interaction during frictional melting.

Additionally, rapid granular flows due to collapse events (e.g., landslides, pyroclastic flows, block-and-ash flows) in materials bearing hydrous minerals could facilitate propagation processes, by decreasing the frictional resistance and thereby increasing the velocity of the flow and its travel distance. Frictional marks on block exteriors from block-and-ash flow deposits have highlighted the highly energetic internal processes taking place within rapid granular flows, where blocks continuously collide and slide past each other (e.g., Grunewald et al., 2000; Schwarzkopf et al., 2001). An investigation of frictional marks found on amphibole-bearing andesitic blocks from Soufrière Hills Volcano (SHV) identified thin pseudotachylyte veins that were compositionally heterogeneous, with SiO_2 ranging from 53 to 63.5 wt.% (Grunewald et al., 2000). The pseudotachylyte glass composition had no overlap with that of the bulk-rock composition and was attributed to matrix melting rather than bulk melting of the host andesite. However, from our findings using a similar andesite from SHV, we suggest pure matrix melting was unlikely and these pseudotachylyte-bearing frictional marks represented very short-lived slip where only the onset of selective phase melting took place rather than prolonged slip to achieve a composition comparable to that of the bulk precursor rock. Contrary to the work of Grunewald et al. (2000), Schwarzkopf et al. (2001) performed a similar chemical analysis on frictional marks imprinted on the surface of andesitic–basaltic-andesite blocks from a block-and-ash flow deposit from Merapi volcano (Indonesia), classifying pseudotachylyte formation as a response to flash melting of the entire rock following frictional contact. This interpretation was based on the consistent compositional overlap of the pseudotachylyte and bulk-rock. From the experiments performed here, the different compositional relationships between the blocks from SHV

and Merapi volcano could be explained by either prolonged sliding of blocks at Merapi (several metres of slip to allow the melt to homogenise towards the bulk-rock composition), prolonged incursion to high temperatures (to favour bulk melting), or a different mineral assemblage. Sustained slip between blocks in a block-and-ash flow is highly unlikely owing to the short-lived, chaotic collisions of rotating blocks; thus, we relate these previously assessed chemical observations to their contrasting bulk mineral assemblages, primarily the high abundance of amphibole in the SHV andesite. We thus anticipate our experimental and geochemical findings will also contribute to the improvement of flow models of similar rapid granular flows, including basal faulting during volcanic avalanches (e.g., Legros et al., 2000; Bernard and de Vries, 2017).

6. Conclusions

We have experimentally demonstrated the effect of contrasting mineral assemblages on the frictional properties of extrusive volcanic rocks, providing a chemical viewpoint to a physical process. We find that the compositional discrepancies in frictional melts are attributed to selective phase melting during faulting, which, in addition to suspended crystal fragments, have a profound influence on the rheological properties of the melt, consequently controlling the mechanical response to slip. Selective melting preferentially occurs in phases with the lowest melting temperatures and mechanical strength, represented by amphibole in the volcanic rocks studied here. In the presence of amphibole, frictional melts are chemically and rheologically complex heterogeneous liquids. With time, these melts homogenise and evolve simultaneously, moving chemically further away from the bulk-rock towards a more mafic composition as amphiboles further from the fault zone continue to melt preferentially. Consequently, the lower melt viscosities attributed to preferential amphibole melting, likely accompanied by H₂O release, facilitate a low shear resistance that promotes slip. When amphibole is absent, frictional melts are compositionally more homogenous from the onset and in general homogenise continuously towards the bulk composition. In this case, the rheological response of the melt is dependent on preferential melting of phases with the next lowest melting temperatures and strength (i.e., plagioclase and rhyolitic glass). High modal fractions of these molten phases lead to frictional melt compositions that are closer to the bulk-rock. Selective melts of these phases have

higher melt viscosities that cause a stronger shear resistance during slip, which may inhibit slip progression but eventually led to failure. These findings provide new insights for assessing volcanic processes that involve slip displacement, either by altering conduit flow dynamics, which could impact the style of an eruption (explosive or effusive), or by contributing to the velocities and run-out distances of rapid granular flows.

Acknowledgments

This work was supported by a European Research Council Starting Grant on ‘Strain Localisation in Magmas’ (SLiM, grant number 306488). Jackie Kendrick was supported by an Early Career Fellowship of the Leverhulme Trust (ECF-2016-325). We acknowledge Diamond Light Source Synchrotron I18 beam time (experiment reference number: SP9220), along with beamline scientists Tina Geraki and Fred Mosselmans for technical support during data acquisition. QEMSCAN data collection was supported by FEI Company of Hillsboro, Oregon, and Richard Worden of the University of Liverpool. We thank Jérémie Vasseur for technical assistance during electron probe microanalysis, Tom Knott for XRF measurements, and Silvio De Angelis and Anthony Lamur for assistance with Matlab script development. We would also like to thank W.U. Reimold and an anonymous reviewer for their helpful reviews.

References

- Allen A. R. (1979) Mechanism of frictional fusion in fault zones. *J. Struct. Geol.* **1**, 231–237.
- Bagdassarov N. S. and Dingwell D. B. (1992) A rheological investigation of vesicular rhyolite. *J. Volcanol. Geotherm. Res.* **50**, 307–322.
- Bernard K. and de Vries B. V. (2017) Volcanic avalanche fault zone with pseudotachylite and gouge in French Massif Central. *J. Volcanol. Geotherm. Res.* **347**, 112–135.
- Caricchi L., Burlini L., Ulmer P., Gerya T., Vassalli M. and Papale P. (2007) Non-Newtonian rheology of crystal-bearing magmas and implications for magma ascent dynamics. *Earth Planet. Sci. Lett.* **264**, 402–419.
- Chen X. F., Madden A. S. E. and Reches Z. (2017) Friction evolution of granitic faults: Heating controlled transition from powder lubrication to frictional melt. *J. Geophys. Res. Solid Earth* **122**, 9275–9289.

Cimarelli C., Costa A., Mueller S. and Mader H. M. (2011) Rheology of magmas with bimodal crystal size and shape distributions: Insights from analog experiments. *Geochem. Geophys.* **12**, Q07024.

Costa A., Caricchi L. and Bagdassarov N. (2009) A model for the rheology of particle-bearing suspensions and partially molten rocks. *Geochem. Geophys.* **10**, Q03010.

De Angelis S. and Henton S. M. (2011) On the feasibility of magma fracture within volcanic conduits: Constraints from earthquake data and empirical modelling of magma viscosity. *Geophys. Res. Lett.* **38**, L19310.

De Campos C. P., Perugini D., Ertel-Ingrisch W., Dingwell D. B. and Poli G. (2011) Enhancement of magma mixing efficiency by chaotic dynamics: an experimental study. *Contrib. Mineral. Petrol.* **161**, 863–881.

Di Toro G., Han R., Hirose T., De Paola N., Nielsen S., Mizoguchi K., Ferri F., Cocco M. and Shimamoto T. (2011) Fault lubrication during earthquakes. *Nature* **471**, 494–498.

Di Toro G., Hirose T., Nielsen S., Pennacchioni G. and Shimamoto T. (2006) Natural and experimental evidence of melt lubrication of faults during earthquakes. *Science* **311**, 647–649.

Dieterich J. H. (1979) Modeling of rock friction. 2. Simulation of pre-seismic slip. *J. Geophys. Res.* **84**, 2169–2175.

Dingwell D. and Webb S. L. (1989) Structural relaxation in silicate melts and Non-Newtonian melt rheology in geologic processes. *Phys. Chem. Miner.* **16**, 508–516.

Fialko Y. and Khazan Y. (2005) Fusion by earthquake fault friction: Stick or slip? *J. Geophys. Res. Solid Earth* **110**, B12407.

Fourcade S. and Allègre C. J. (1981) Trace-elements behavior in granite genesis - a case-study the calc-alkaline plutonic association from the Querigut Complex (Pyrenees, France). *Contrib. Mineral. Petrol.* **76**, 177–195.

Francis P. W. (1972) The pseudotachylyte problem. *Comments Earth Sci. Geophys.* **3**, 35–53.

Giordano D., Romano C., Dingwell D. B., Poe B. and Behrens H. (2004) The combined effects of water and fluorine on the viscosity of silicic magmas. *Geochim. Cosmochim. Acta* **68**, 5159–5168.

Giordano D., Russell J. K. and Dingwell D. B. (2008) Viscosity of magmatic liquids: A model. *Earth Planet. Sci. Lett.* **271**, 123–134.

- Gottlieb P., Wilkie G., Sutherland D., Ho-Tun E., Suthers S., Perera K., Jenkins B., Spencer S., Butcher A. and Rayner J. (2000) Using quantitative electron microscopy for process mineralogy applications. *Journal of the Minerals, Metals & Materials Society* **52**, 24–25.
- Grunewald U., Sparks R. S. J., Kearns S. and Komorowski J. C. (2000) Friction marks on blocks from pyroclastic flows at the Soufrière Hills volcano, Montserrat: Implications for flow mechanisms. *Geology* **28**, 827–830.
- Hale A. J. and Wadge G. (2008) The transition from endogenous to exogenous growth of lava domes with the development of shear bands. *J. Volcanol. Geotherm. Res.* **171**, 237–257.
- Harbord C. W. A., Nielsen S. B., De Paola N. and Holdsworth R. E. (2017) Earthquake nucleation on rough faults. *Geology* **45**, 931–934.
- Harford C. L., Sparks R. S. J. and Fallick A. E. (2003) Degassing at the Soufrière Hills Volcano, Montserrat, recorded in matrix glass compositions. *J. Petrol.* **44**, 1503–1523.
- Herrmann W. and Berry R. F. (2002) MINSQ - a least squares spreadsheet method for calculating mineral proportions from whole rock major element analyses. *Geochem. Explor. Env. A.* **2**, 361–368.
- Hess K. U. and Dingwell D. B. (1996) Viscosities of hydrous leucogranitic melts: a non-Arrhenian model. *Am. Mineral.* **81**, 1297–1300.
- Hetzel R., Altenberger U. and Strecker M. R. (1996) Structural and chemical evolution of pseudotachylytes during seismic events. *Miner. Petrol.* **58**, 33–50.
- Hirose T. and Shimamoto T. (2003) Fractal dimension of molten surfaces as a possible parameter to infer the slip-weakening distance of faults from natural pseudotachylytes. *J. Struct. Geol.* **25**, 1569–1574.
- Hirose T. and Shimamoto T. (2005) Growth of molten zone as a mechanism of slip weakening of simulated faults in gabbro during frictional melting. *J. Geophys. Res. Solid Earth* **110**, B05202.
- Hornby A. J., Kendrick J. E., Lamb O. D., Hirose T., De Angelis S., von Aulock F. W., Umakoshi K., Miwa T., Henton De Angelis S., Wadsworth F. B., Hess K. U., Dingwell D. B. and Lavallée Y. (2015) Spine growth and seismogenic faulting at Mt. Unzen, Japan. *J. Geophys. Res. Solid Earth* **120**, 4034–4054.
- Horwell C., Williamson B., Llewellyn E., Damby D. and Blond J. (2013) The nature and formation of cristobalite at the Soufrière Hills volcano, Montserrat: implications for the petrology and stability of silicic lava domes. *Bull. Volcanol.* **75**, 1–19.
- Hu W., Huang R. Q., McSaveney M., Zhang X. H., Yao L. and Shimamoto T. (2018) Mineral changes quantify frictional heating during a large low-friction landslide. *Geology* **46**, 223–226.

- Humphreys M. C. S., Edmonds M., Christopher T. and Hards V. (2009) Chlorine variations in the magma of Soufriere Hills Volcano, Montserrat: Insights from Cl in hornblende and melt inclusions. *Geochim. Cosmochim. Acta* **73**, 5693–5708.
- Huppert H. E. and Sparks S. J. (1984) Double-diffusive convection due to crystallization in magmas. *Annu. Rev. Earth Planet. Sci.* **12**, 11–37.
- Jiang H. H., Lee C. T. A., Morgan J. K. and Ross C. H. (2015) Geochemistry and thermodynamics of an earthquake: A case study of pseudotachylites within mylonitic granitoid. *Earth Planet. Sci. Lett.* **430**, 235–248.
- Johnson J. B., Lees J. M., Gerst A., Sahagian D. and Varley N. (2008) Long-period earthquakes and co-eruptive dome inflation seen with particle image velocimetry. *Nature* **456**, 377–381.
- Kendrick J. E., Lavallée Y., Ferk A., Perugini D., Leonhardt R. and Dingwell D. B. (2012) Extreme frictional processes in the volcanic conduit of Mount St. Helens (USA) during the 2004–2008 eruption. *J. Struct. Geol.* **38**, 61–76.
- Kendrick J. E., Lavallée Y., Hess K. U., De Angelis S., Ferk A., Gaunt H. E., Meredith P. G., Dingwell D. B. and Leonhardt R. (2014a) Seismogenic frictional melting in the magmatic column. *Solid Earth* **5**, 199–208.
- Kendrick J. E., Lavallée Y., Hirose T., Di Toro G., Hornby A. J., De Angelis S. and Dingwell D. B. (2014b) Volcanic drumbeat seismicity caused by stick-slip motion and magmatic frictional melting. *Nat. Geosci.* **7**, 438–442.
- Kirkpatrick J. D. and Rowe C. D. (2013) Disappearing ink: How pseudotachylites are lost from the rock record. *J. Struct. Geol.* **52**, 183–198.
- Koizumi Y., Otsuki K., Takeuchi A. and Nagahama H. (2004) Frictional melting can terminate seismic slips: Experimental results of stick-slips. *Geophys. Res. Lett.* **31**, L21605.
- Lavallée Y., Benson P. M., Heap M. J., Hess K. U., Flaws A., Schillinger B., Meredith P. G. and Dingwell D. B. (2013) Reconstructing magma failure and the degassing network of dome-building eruptions. *Geology* **41**, 515–518.
- Lavallée Y., Dingwell D. B., Johnson J. B., Cimarelli C., Hornby A. J., Kendrick J. E., von Aulock F. W., Kennedy B. M., Andrews B. J., Wadsworth F. B., Rhodes E. and Chigna G. (2015a) Thermal vesiculation during volcanic eruptions. *Nature* **528**, 544–547.
- Lavallée Y., Hirose T., Kendrick J. E., De Angelis S., Petrakova L., Hornby A. J. and Dingwell D. B. (2014) A frictional law for volcanic ash gouge. *Earth Planet. Sci. Lett.* **400**, 177–183.

Lavallée Y., Hirose T., Kendrick J. E., Hess K. U. and Dingwell D. B. (2015b) Fault rheology beyond frictional melting. *Proc. Natl. Acad. Sci. U.S.A* **112**, 9276–9280.

Lavallée Y., Mitchell T. M., Heap M. J., Vasseur J., Hess K. U., Hirose T. and Dingwell D. B. (2012) Experimental generation of volcanic pseudotachylytes: Constraining rheology. *J. Struct. Geol.* **38**, 222–233.

Lee S. K., Han R., Kim E. J., Jeong G. Y., Khim H. and Hirose T. (2017) Quasi-equilibrium melting of quartzite upon extreme friction. *Nat. Geosci.* **10**, 436–441.

Legros F., Cantagrel J. M. and Devouard B. (2000) Pseudotachylyte (frictionite) at the base of the Arequipa volcanic landslide deposit (Peru): Implications for emplacement mechanisms. *J. Geol.* **108**, 601–611.

Lin A. M. (1999) Roundness of clasts in pseudotachylytes and cataclastic rocks as an indicator of frictional melting. *J. Struct. Geol.* **21**, 473–478.

Lin A. M. and Shimamoto T. (1998) Selective melting processes as inferred from experimentally generated pseudotachylytes. *J. Asian Earth Sci.* **16**, 533–545.

Lockner D. A., Kilgore B. D., Beeler N. M. and Moore D. E. (2017) The transition from frictional sliding to shear melting in laboratory stick-slip experiments, in: Thomas, M., Mitchell, T., Bhat, H. (Eds.), *Fault zone dynamic processes: Evolution of fault properties during seismic rupture*. American Geophysical Union, Washington, DC, pp. 105–132.

Luhr J. F. (2002) Petrology and geochemistry of the 1991 and 1998–1999 lava flows from Volcán de Colima, México: implications for the end of the current eruptive cycle. *J. Volcanol. Geotherm. Res.* **117**, 169–194.

Luhr J. F. and Carmichael I. S. E. (1990) Petrological monitoring of cyclical eruptive activity at Volcán Colima, Mexico. *J. Volcanol. Geotherm. Res.* **42**, 235–260.

Macias J. L., Sosa-Ceballos G., Arce J. L., Gardner J. E., Saucedo R. and Valdez-Moreno G. (2017) Storage conditions and magma processes triggering the 1818 CE Plinian eruption of Volcán de Colima. *J. Volcanol. Geotherm. Res.* **340**, 117–129.

Mader H., Llewellyn E. and Mueller S. (2013) The rheology of two-phase magmas: A review and analysis. *J. Volcanol. Geotherm. Res.* **257**, 135–158.

Magloughlin J. F. (1992) Microstructural and chemical-changes associated with cataclasis and frictional melting at shallow crustal levels - the cataclasite pseudotachylyte connection. *Tectonophysics* **204**, 243–260.

Magloughlin J. F. and Spray J. G. (1992) Frictional Melting Processes and Products in Geological-Materials - Introduction and Discussion. *Tectonophysics* **204**, 197–206.

McKenzie D. and Brune J. N. (1972) Melting on fault planes during large earthquakes. *Geophys. J. Roy. Astron. Soc.* **29**, 65–78.

Morgavi D., Perugini D., De Campos C. P., Ertel-Ingrisch W. and Dingwell D. B. (2013) Time evolution of chemical exchanges during mixing of rhyolitic and basaltic melts. *Contrib. Mineral. Petrol.* **166**, 615–638.

Mueller S., Llewellyn E. W. and Mader H. M. (2011) The effect of particle shape on suspension viscosity and implications for magmatic flows. *Geophys. Res. Lett.* **38**, L13316.

Murphy M. D., Sparks R. S. J., Barclay J., Carroll M. R. and Brewer T. S. (2000) Remobilization of andesite magma by intrusion of mafic magma at the Soufrière Hills Volcano, Montserrat, West Indies. *J. Petrol.* **41**, 21–42.

Neuberg J. W., Tuffen H., Collier L., Green D., Powell T. and Dingwell D. (2006) The trigger mechanism of low-frequency earthquakes on Montserrat. *J. Volcanol. Geotherm. Res.* **153**, 37–50.

Nielsen S., Di Toro G. and Griffith W. A. (2010) Friction and roughness of a melting rock surface. *Geophysical Journal International* **182**, 299–310.

Nielsen S., Di Toro G., Hirose T. and Shimamoto T. (2008) Frictional melt and seismic slip. *Journal of Geophysical Research-Solid Earth* **113**, B01308.

Niemeijer A. R., Di Toro G., Nielsen S. and Di Felice F. (2011) Frictional melting of gabbro under extreme experimental conditions of normal stress, acceleration and sliding velocity. *J. Geophys. Res. Solid Earth* **116**, B07404.

O'Hara K. D. (1992) Major- and trace-element constraints on the petrogenesis of a fault-related pseudotachylyte, western Blue Ridge Province, North Carolina. *Tectonophysics* **204**, 279–288.

Ohmura A. and Kawamura H. (2007) Rate- and state-dependent friction law and statistical properties of earthquakes. *Europhys. Lett.* **77**, 69001.

Perugini D., De Campos C. P., Dingwell D. B. and Dorfman A. (2013) Relaxation of concentration variance: A new tool to measure chemical element mobility during mixing of magmas. *Chem. Geol.* **335**, 8–23.

Perugini D., De Campos C. R., Dingwell D. B., Petrelli M. and Poli G. (2008) Trace element mobility during magma mixing: Preliminary experimental results. *Chem. Geol.* **256**, 146–157.

- Perugini D., Petrelli M. and Poli G. (2006) Diffusive fractionation of trace elements by chaotic mixing of magmas. *Earth Planet. Sci. Lett.* **243**, 669–680.
- Perugini D., Poli G. and Mazzuoli R. (2003) Chaotic advection, fractals and diffusion during mixing of magmas: evidence from lava flows. *J. Volcanol. Geotherm. Res.* **124**, 255–279.
- Popov V. L., Grzemba B., Starcevic J. and Popov M. (2012) Rate and state dependent friction laws and the prediction of earthquakes: What can we learn from laboratory models? *Tectonophysics* **532**, 291–300.
- Pouchou J. L. and Pichoir F. (1984) A new model for quantitative X-ray-microanalysis .1. Application to the analysis of homogeneous samples. *Rech. Aéropat.*, 167–192.
- Reches Z. and Lockner D. A. (2010) Fault weakening and earthquake instability by powder lubrication. *Nature* **467**, 452–455.
- Reubi O. and Blundy J. (2008) Assimilation of plutonic roots, formation of high-K ‘exotic’ melt inclusions and genesis of andesitic magmas at Volcán De Colima, Mexico. *J. Petrol.* **49**, 2221–2243.
- Rice J. R., Lapusta N. and Ranjith K. (2001) Rate and state dependent friction and the stability of sliding between elastically deformable solids. *J. Mech. Phys. Solids* **49**, 1865–1898.
- Rose W. I. (1972) Santiaguito Volcanic Dome, Guatemala. *Geol. Soc. Am. Bull.* **83**, 1413–1434.
- Rosenberg C. L. and Handy M. R. (2005) Experimental deformation of partially melted granite revisited: implications for the continental crust. *J. Metamorph. Geol.* **23**, 19–28.
- Rossi S., Petrelli M., Morgavi D., Gonzalez-Garcia D., Fischer L. A., Vetere F. and Perugini D. (2017) Exponential decay of concentration variance during magma mixing: Robustness of a volcanic chronometer and implications for the homogenization of chemical heterogeneities in magmatic systems. *Lithos* **286**, 396–407.
- Rust A. C. and Manga M. (2002) Bubble Shapes and Orientations in Low Re Simple Shear Flow. *Journal of Colloid and Interface Science* **249**, 476–480.
- Saucedo R., Macias J. L., Gavilanes J. C., Arce J. L., Komorowski J. C., Gardner J. E. and Valdez-Moreno G. (2010) Eyewitness, stratigraphy, chemistry, and eruptive dynamics of the 1913 Plinian eruption of Volcán de Colima, México. *J. Volcanol. Geotherm. Res.* **191**, 149–166.
- Savov I. P., Luhr J. F. and Navarro-Ochoa C. (2008) Petrology and geochemistry of lava and ash erupted from Volcán Colima, Mexico, during 1998–2005. *J. Volcanol. Geotherm. Res.* **174**, 241–256.

Schneider C. A., Rasband W. S. and Eliceiri K. W. (2012) NIH Image to ImageJ: 25 years of image analysis. *Nat. Methods* **9**, 671–675.

Schwarzkopf L. M., Schmincke H. U. and Troll V. R. (2001) Pseudotachylite on impact marks of block surfaces in block-and-ash flows at Merapi volcano, Central Java, Indonesia. *Int. J. Earth Sci.* **90**, 769–775.

Scott J. A. J., Pyle D. M., Mather T. A. and Rose W. I. (2013) Geochemistry and evolution of the Santiaguito volcanic dome complex, Guatemala. *J. Volcanol. Geotherm. Res.* **252**, 92–107.

Scott J. S. and Drever H. I. (1953) Frictional fusion along a Himalayan thrust. *P. Roy. Soc. Edinb.* **658**, 121–142.

Shand S. J. (1916) The pseudotachylite of Parijs (Orange Free State), and its relation to “trap-shotten gneiss” and “flinty crush-rock”. *Q. J. Geol. Soc.* **72**, 198–221.

Shimamoto T. and Lin A. (1994) Is frictional melting equilibrium melting, or non-equilibrium melting? *Struct. Geol. J. Tectonic Res. Group Jpn.* **39**, 79–84.

Shimamoto T. and Tsutsumi A. (1994) A new rotary-shear high-speed frictional testing machine: its basic design and scope of research. *Structural Geology: Journal of the Tectonic Research Group of Japan* **39**, 65–78.

Sibson R. H. (1975) Generation of pseudotachylite by ancient seismic faulting. *J. Roy. Astron. Soc. London* **43**, 775–794.

Spagnuolo E., Nielsen S., Violay M. and Di Toro G. (2016) An empirically based steady state friction law and implications for fault stability. *Geophys. Res. Lett.* **43**, 3263–3271.

Sparks R. S. J. and Marshall L. A. (1986) Thermal and mechanical constraints on mixing between mafic and silicic magmas. *J. Volcanol. Geotherm. Res.* **29**, 99–124.

Spray J. G. (1992) A physical basis for the frictional melting of some rock-forming minerals. *Tectonophysics* **204**, 205–221.

Tsutsumi A. and Shimamoto T. (1997) High-velocity frictional properties of gabbro. *Geophys. Res. Lett.* **24**, 699–702.

Tuffen H. and Dingwell D. (2005) Fault textures in volcanic conduits: evidence for seismic trigger mechanisms during silicic eruptions. *Bull. Volcanol.* **67**, 370–387.

Violay M., Di Toro G., Gibert B., Nielsen S., Spagnuolo E., Del Gaudio P., Azais P. and Scarlato P. G. (2014) Effect of glass on the frictional behavior of basalts at seismic slip rates. *Geophys. Res. Lett.* **41**, 348–355.

Wallace P. A., Kendrick J. E., Ashworth J. D., Miwa T., Coats R., Henton De Angelis S., Mariani E., Utley J., Biggin A., Kendrick R., Nakada S., Matsushima T. and Lavallée Y. (2019) Petrological architecture of a magmatic shear zone: A multidisciplinary investigation of strain localisation during magma ascent at Unzen Volcano, Japan. *J. Petrol.*, DOI: 10.1093/petrology/egz1016.

Webb S. L. and Dingwell D. B. (1990) Non-Newtonian rheology of igneous melts at high stresses and strain rates: experimental results for rhyolite, andesite, basalt and nephelinite. *J. Geophys. Res.* **95**, 15695–15701.

ACCEPTED MANUSCRIPT

Tables

Table 1: Geochemical compositions of the bulk starting materials (measured by XRF) and interstitial glass (measured by electron probe microanalysis).

Location:	Soufrière Hills Volcano		Santiaguito dome complex		Volcán de Colima	
Sample:	SHV		SG		COL	
Rock type:	Andesite		Dacite		Andesite	
Deposit:	Dome collapse		Lava spine		Dome collapse	
	Bulk-rock	Glass	Bulk-rock	Glass	Bulk-rock	Glass
(wt.%)	<i>n</i> 14		<i>n</i> 9		<i>n</i> 19	
SiO ₂	59.59	79.72 (4.82)	64.44	75.65 (1.38)	62.05	77.00 (0.71)
TiO ₂	0.60	0.29 (0.09)	0.42	0.44 (0.05)	0.51	0.56 (0.06)
Al ₂ O ₃	18.49	10.93 (2.91)	17.66	12.27 (0.79)	17.74	11.35 (0.38)
FeO*	6.13	1.32 (0.50)	4.06	1.81 (0.46)	4.58	1.86 (0.11)
MnO	0.16	<lld	0.14	<lld	0.10	<lld
MgO	2.74	0.18 (0.26)	1.67	0.30 (0.27)	2.83	0.16 (0.06)
CaO	7.76	2.20 (1.10)	4.61	0.45 (0.29)	5.59	0.48 (0.13)
Na ₂ O	3.34	3.23 (0.63)	4.79	3.88 (0.54)	4.48	4.04 (0.22)
K ₂ O	0.80	1.91 (0.64)	1.70	4.95 (0.34)	1.32	4.27 (0.33)
P ₂ O ₅	0.13	<lld	0.21	<lld	0.18	<lld
Cl	-	0.08 (0.04)	-	0.11 (0.04)	-	0.12 (0.03)
LOI	0.07	-	0.18	-	0.15	-
Total [§]	99.81	100.84	99.88	99.32	99.53	99.72
(ppm)						
Ba	214	-	805	-	618	-
Ce	26	-	26	-	30	-
La	13	-	16	-	11	-
Nb	3	-	6	-	3	-
Nd	14	-	16	-	16	-
Pb	3	-	8	-	6	-
Rb	17	-	32	-	19	-
Sc	16	-	8	-	12	-
Sr	278	-	470	-	601	-
Th	2	-	2	-	1	-
V	131	-	53	-	97	-
Y	24	-	17	-	14	-
Zn	56	-	73	-	53	-
Zr	99	-	154	-	124	-

All oxide concentrations are normalised averages of *n* measurements. Values in parentheses are standard deviations (1σ) from *n* analyses. See Electronic Annex for all measurements.

[§] Original total

* All Fe as FeO

<lld, below lower limit of detection

Table 2: Quantitative mineral modal abundance for the bulk starting materials and the host groundmass.

Location:	Soufrière Hills Volcano		Santiaguito dome complex		Volcán de Colima	
Sample:	SHV		SG		COL	
Rock type:	Andesite		Dacite		Andesite	
Deposit:	Dome collapse		Lava spine		Dome collapse	
<i>(vol.%)</i>	Bulk- rock ^a	Groundmass ^b	Bulk- rock ^a	Groundmass ^b	Bulk- rock ^a	Groundmass ^b
Plagioclase	52.5	27.4	63.9	38.8	67.0	30.0
Amphibole	9.3	0.0	1.5	0.0	1.1	0.0
Orthopyroxene	6.4	16.8 ^d	2.9	2.6 ^d	6.5	3.8 ^d
Clinopyroxene	2.3		0.3		1.2	
Si polymorph^c	13.0	23.2	14.2	11.0	5.6	2.0
Fe-Ti oxide	1.9	3.4	1.0	1.4	0.8	2.2
Apatite	0.3	-	0.4	-	0.4	-
Olivine	0.0	0.0	0.0	0.0	Rare	0.0
Glass	14.4	19.2	15.9	46.2	17.2	62.0
Vesicularity	15.2	10.0	7.0	0.0	13.7	0.0
Porosity (Pyc)^e	13.0	n.a.	9.0	n.a.	17.0	n.a.

^a Bulk mineralogy acquired from QEMSCAN

^b Groundmass mineralogy determined using point counting

^c Combines quartz, cristobalite, and tridymite

^d Groundmass pyroxene abundances combines both orthopyroxene and clinopyroxene.

^e Connected porosities measured by He-pycnometry using cores from each starting material

Table 3: A summary of the experimental conditions along with mechanical and rheological data measured for each high-velocity rotary shear (HVR) experiment: SHV = Soufrière Hills Volcano andesite; COL = Volcán de Colima andesite; SG = Santiaguito dome complex dacite.

Experiment	Max. shear stress (MPa) ^a	Steady-state shear stress (MPa) ^a	Total slip distance (m)	Total shortening (mm)	Melt zone thickness (avg.; mm) ^b	Crystal fraction ^c	RPM	Outer diameter (mm)	Inner diameter (mm)	V_e (Rotation Velocity; m s ⁻¹) ^d	($\dot{\epsilon}$) Strain-rate (s ⁻¹) ^e	Relative viscosity (Log Pa s) ^f	HVR apparent viscosity (Log Pa s) ^g
SHV T _m	1.08	-	10.8	0.00	0.30	0.32	1043	24.94	9.32	1.00	4.1E+03	0.55	-
SHV T _{ss}	1.25	0.92	16.7	0.08	0.30	0.30	1044	24.96	9.27	1.00	6.4E+03	0.50	2.16
SHV T ₅	1.27	0.88	17.6	0.18	0.30	0.38	1044	24.97	9.29	1.00	6.8E+03	0.72	2.11
SHV T ₁₀	1.24	0.87	25.5	0.46	0.30	0.44	1044	24.96	9.30	1.00	9.8E+03	0.97	1.95
SHV T ₁₅	1.34	0.88	27.2	1.43	0.30	0.43	1044	24.94	9.26	1.00	1.0E+04	0.92	1.93
COL T _m	1.07	-	9.30	0.01	0.25	0.36	1047	24.97	9.02	1.00	4.3E+03	0.65	-
COL T _{ss}	1.12	0.73	12.1	0.01	0.55	0.24	1047	24.96	9.13	1.00	2.5E+03	0.36	2.46
COL T ₅	1.88	1.50	18.1	1.49	0.55	0.40	1044	24.97	9.25	1.00	3.8E+03	0.79	2.60
COL T ₁₀	2.11	1.68	23.0	3.34	0.55	0.35	1047	24.98	9.19	1.00	4.8E+03	0.63	2.54
COL T ₁₅	2.00	1.70	32.2	5.53	0.50	0.35	1044	24.95	9.20	1.00	7.4E+03	0.63	2.36
SG T _m	1.30	-	16.0	0.11	0.35	0.20	1046	24.96	9.12	1.00	5.2E+03	0.28	-
SG T _{ss}	1.89	1.78	21.9	0.29	0.50	0.21	1044	24.99	9.18	1.00	5.0E+03	0.30	2.55
SG T ₅	1.78	1.44	21.9	1.05	0.45	0.30	1053	24.83	8.98	1.00	5.5E+03	0.50	2.41
SG T ₁₀	1.90	1.71	27.3	3.39	0.45	0.26	1035	24.96	9.72	1.00	7.0E+03	0.40	2.39
SG T ₁₅	1.91	1.70	31.4	5.22	0.45	0.24	1044	24.94	9.28	1.00	8.0E+03	0.36	2.33

^a Maximum and steady-state shear stress values are an average of the peak and steady-state portion of the curves in Fig. A1–3, respectively.

^b Melt zone thickness estimated from optical images and averaged using multiple transects perpendicular to the slip surface; to ensure accuracy, measurements were only taken where melt was in direct contact with the bulk material on both sides.

^c Crystal fractions quantified using SEM-BSE images of the melt.

^d Equivalent rotation velocities (V_e) were used to calculate displacement rates (Eq. 4) after Shimamoto and Tsutsumi (1994).

^e Strain-rates ($\dot{\epsilon}$) were calculated for slip during steady-state conditions (Eq. 2) using an equivalent diameter (D_e ; Eq. 3), melt thickness, and slip duration.

^f Relative effect of crystals suspended within the frictional melt on melt viscosities were estimated by applying the method of Costa et al. (2009) and the parameterised experimental data of Caricchi et al. (2007), using measured crystal fractions and calculated strain-rate data.

^g HVR apparent viscosities were calculated from the mechanical data using Eq. 1 for steady-state conditions.

Figure captions

Fig. 1: Mineralogical and textural characteristics of the three host materials used in the high-velocity rotary shear (HVR) experiments: Soufrière Hills Volcano (SHV) andesite (a–c), Santiaguito dome complex (SG) dacite (d–f), and Volcán de Colima (COL) andesite (g–i). Panels (a, d and g) are photographs of the cored starting materials, (b, e and h) are QEMSCAN maps used for quantifying bulk-rock phase abundances, where colours identify phases as shown in the key and white indicates pore space, and (c, f and i) are backscattered electron (BSE) images showing groundmass textures. The phases in the groundmass include plagioclase (Pl), pyroxenes (Px), oxides (Ox), silica polymorphs (Si), and interstitial glass (Gl).

Fig. 2: Visual and mechanical observations of frictional melt evolution of the Soufrière Hills Volcano (SHV) andesite, Santiaguito dome complex (SG) dacite, and Volcán de Colima (COL) andesite. (a) Freeze-frames of optical recordings of the simulated fault zone upon stopping the experiment at T_m (melting onset), T_5 (5 m of slip at steady-state conditions), and T_{15} (15 m of slip at steady-state conditions). The time (t) refers to the total duration of the experiment. (b) Mechanical data showing the different slip behaviours of the three starting materials, including evolution in shear stress (τ) and experimental sample shortening. Only the mechanical data for T_{15} experiments are displayed for comparison (see Fig. A1–A3 for all data). (c) Timeline displaying different stages of frictional melting: onset of melting (T_m), reaching steady-state conditions (T_{ss}), 5 m slip at steady-state (T_5), and 10 m slip at steady-state (T_{10}), with all data derived from the T_{15} experiment in (b).

Fig. 3: Backscattered electron (BSE) images showing the microtextural evolution of frictional melts from the onset of melting (T_m) to 15 m of slip at steady-state conditions (T_{15}) for each starting material. The inset text shows the fraction of melt and crystals, along with the percentage porosity of the frictional melt layer (pores/bubbles were defined using a >0.8 circularity threshold in imageJ). Labelled phases include: plagioclase (Pl), pyroxenes (Px), oxides (Ox), silica polymorphs (Si), and interstitial glass (Gl), in addition to bubbles (Bl.) in the melt zone. ‘Rim’ denotes examples of partially resorbed crystal edges.

Fig. 4: Binary plots showing the evolution in frictional melt composition for representative major element oxides (SiO_2 , CaO, FeO, MgO, Al_2O_3 , and Na_2O) with increasing slip displacement from the onset of melting (T_m) to 15 m of steady-state (SS) slip after melting (T_{15}). (a) Soufrière Hills Volcano (SHV) andesite, (b) Santiaguito dome complex (SG) dacite, and (c) Volcán de Colima (COL) andesite. For comparison, the composition of host-rock plagioclase, interstitial glass, and amphibole (for SHV only) are plotted, along with the composition of each bulk starting material.

Fig. 5: Standard deviations (σ) of compositional variability for the experimental frictional melts as a function of slip distance from the onset of melting (T_m) to 15 m of slip at steady-state conditions (T_{15}) for the different major components (a–f). The σ for each component decreases with slip duration for all starting materials, modelled using an exponential fit of the data. Frictional melts derived from the Soufrière Hills Volcano (SHV) andesite have the highest σ for all major components, while melts from Santiaguito dome complex (SG) dacite and Volcán de Colima (COL) andesite have the lowest.

Fig. 6: Amphibole-melt interaction during frictional melting of the Soufrière Hills Volcano (SHV) andesite. (a) Backscattered electron (BSE) image of the frictional melt zone after 15 m of slip at steady-state conditions (T_{15}), displaying both an amphibole and plagioclase phenocryst on the right side of the melt zone, and groundmass on the left side of the melt zone. (b) BSE image emphasising the nature of the contact between the amphibole and the melt zone displaying textural alteration of the amphibole. (c) Composition of the frictional melt and amphibole phenocryst along the transect labelled by the arrow in (b). (d) Synchrotron X-ray spectroscopy element maps of the amphibole-melt contact as shown in (b).

Fig. 7: Synchrotron X-ray element maps of Volcán de Colima (COL) andesite frictional melt after 10 m of slip at steady-state conditions (T_{10}). The backscattered electron (BSE) image shows the contact between the frictional melt and the host-rock groundmass. The element maps are taken from the outlined area of the BSE image (red box) and depict the contribution of interstitial glass and other groundmass phases to frictional melt composition. Interstitial glass is identified by the highest concentrations of K, Rb, and Zr.

Fig. 8: Box plots showing the contribution of the different minerals and glass phases to the frictional melt composition calculated using the least squares petrological mixing program MINSQ (Herrmann and Berry, 2002). The phases contributing to the frictional melt derived from Soufrière Hills Volcano (SHV) andesite, Santiaguito dome complex (SG) dacite, and Volcán de Colima (COL) andesite, include: (a) amphibole (hornblende), (b) plagioclase, (c) interstitial glass, (d) orthopyroxene (hypersthene), (e) clinopyroxene (augite), and (f) Fe-Ti oxides. All estimated phase abundances are compared to the respective abundances of the host rocks. Outliers were detected using the interquartile range (IQR) rule.

Fig. 9: Non-Arrhenian temperature dependence of viscosity of the experimental frictional melts. Viscosities were calculated using the GRD viscosity model of Giordano et al. (2008) for melts derived

from the frictional melting of (a) Soufrière Hills Volcano (SHV) andesite, (b) Santiaguito dome complex (SG) dacite, and (c) Volcàn de Colima (COL) andesite. The chemical compositions of the frictional melts, derived by electron probe microanalysis, were used as input parameters, including the most mafic and felsic melts from the onset of melting (T_m) and the homogenised frictional melts after 15 m of steady-state slip (T_{15}). The relative effect of crystals on melt viscosity was modelled considering crystal fraction and strain-rate following the method of Costa et al. (2009); these relative viscosities were added to the homogenised melt curves to produce a modelled apparent viscosity. The modelled apparent viscosities of the frictional melt suspensions were compared with the mechanically constrained apparent viscosities (Eq. 1; $T_{\text{Monitored}}$), providing an estimated temperature of the frictional melt zone ($T_{\text{Estimated}}$). (d) Effect of different water contents on the apparent viscosity of SHV frictional melt owing to the presence of hydrous amphibole melting. The red line indicates 0.5 wt.% H_2O based on 27 vol.% amphibole melting for frictional melts at T_{15} .

Fig. A1: Mechanical data for the five high-velocity rotary shear (HVR) experiments performed on the Soufrière Hills Volcano (SHV) andesite. Each panel represents the evolution in frictional properties (i.e., shear stress, normal stress and sample shortening) monitored during experiments that were terminated at: (a) onset of melting (T_m), (b) formation of full frictional melt and attainment of steady-state condition (T_{ss}), (c) after 5 m of slip at steady-state conditions (T_5), (d) after 10 m of slip at steady-state conditions (T_{10}), and (e) after 15 m of slip at steady-state conditions (T_{15}).

Fig. A2: Mechanical data for the five high-velocity rotary shear (HVR) experiments performed on the Santiaguito dome complex (SG) dacite. Each panel represents the evolution in frictional properties (i.e., shear stress, normal stress and sample shortening) monitored during experiments that were terminated at: (a) onset of melting (T_m), (b) formation of full frictional melt and attainment of steady-state condition (T_{ss}), (c) after 5 m of slip at steady-state conditions (T_5), (d) after 10 m of slip at steady-state conditions (T_{10}), and (e) after 15 m of slip at steady-state conditions (T_{15}).

Fig. A3: Mechanical data for the five high-velocity rotary shear (HVR) experiments performed on the Volcàn de Colima (COL) andesite. Each panel represents the evolution in frictional properties (i.e., shear stress, normal stress and sample shortening) monitored during experiments that were terminated at: (a) onset of melting (T_m), (b) formation of full frictional melt and attainment of steady-state condition (T_{ss}), (c) after 5 m of slip at steady-state conditions (T_5), (d) after 10 m of slip at steady-state conditions (T_{10}), and (e) after 15 m of slip at steady-state conditions (T_{15}). Note that steady-state melting in (b) occurred at a shorter slip distance than the onset of melting in (a), which demonstrates the natural variability of a single sample.

Fig. A4: Major element chemical transects across the experimental melt zone (i.e., perpendicular to the slip plane) following melting of the (a) Soufrière Hills Volcano (SHV) andesite, (b) Santiaguito dome complex (SG) dacite and (c) Volcán de Colima (COL) andesite at: onset of melting (T_m), formation of full frictional melt and attainment of steady-state condition (T_{ss}), and after 5 m (T_5), 10 m (T_{10}), and 15 m of slip at steady-state conditions (T_{15}). The composition of the bulk-rock along with averages of the bulk-rock interstitial glass and plagioclase crystals have been labelled for reference.

Fig. A5: Synchrotron X-ray element maps of Soufrière Hills Volcano (SHV) frictional melt formed after 5 m of slip at steady-state conditions (T_5) displaying the contribution of amphibole to frictional melt composition. Elements that are high in concentration in amphiboles include: Ca, Fe and Y; amphibole incompatible elements include: K, Sr, Rb, and Zr.

Fig. A6: Synchrotron X-ray element maps of Soufrière Hills Volcano (SHV) frictional melt upon reaching steady-state conditions (T_{ss}) displaying the contributions of plagioclase (left of maps) and clinopyroxene (augite; right of maps) to frictional melt composition.

Fig. A7: Synchrotron X-ray element maps of Santiaguito dome complex (SG) frictional melt upon reaching steady-state conditions (T_{ss}) displaying the contributions of orthopyroxene (OPX, hypersthene; top right of map) and interstitial glass (bottom of maps) to frictional melt composition.

